Characterizing sudden changes in Arctic sea ice drift and deformation on synoptic timescales

J.V. Lukovich[1], C.A. Geiger[2], D.G. Barber[1]

[1]Centre for Earth Observation Science, University of Manitoba, Winnipeg, R3T 2N2, CANADA
[2]College of Earth, Ocean, and Environment: Geography, University of Delaware, Delaware, 19716, USA

Correspondence to: J.V. Lukovich (Jennifer.Lukovich@umanitoba.ca)

Abstract. In this study, we develop a framework for the assessment of sudden changes in sea ice drift paths and associated deformation processes in response to atmospheric forcing, based on a Lagrangian statistical analysis of ice buoy triplet centroids and areas. Examined in particular is the spatiotemporal evolution in sea ice floes that are tracked with GPS beacons deployed in triplets in the southern Beaufort Sea at varying distances from the coastline in fall, 2009 – triplets A to D, with A (D) located closest to (furthest from) the coastline. This study illustrates the use of diagnostics to evaluate eight identified sudden changes or shock events on daily timescales. Results from this analysis show that single-particle (absolute) dispersion provides a characterization of regional changes in the sea ice cover in response to atmospheric forcing, while two- (relative) and three-particle dispersion statistics provide a characterization of local changes associated with sea ice deformation. Demonstrated in particular is a change in sea ice dynamics following a SLP high on 8 October, 2009, evident in a transition from absolute dispersion scaling exponents of $\alpha \sim 3$ to 2, and accompanying loss of synchronicity in ice-atmosphere interactions. Results from two- and three-particle dispersion statistics highlight differences in sea ice deformation based on distance from the coastline. The tools developed in this study provide a unique characterization of sea ice dynamical processes in the southern Beaufort Sea based on Lagrangian, and in particular one-, two-, and three-particle dispersion statistics, with implications for quantifying sudden changes relevant for ice hazard assessments and forecasting applications required by oil and gas, marine transportation, and indigenous use of near shore Arctic areas.

Deleted: and ice-coastal interactions

Deleted: shock-response

Deleted: shock events in the southern Beaufort Sea occur in at least one of two forms: (1) during a reversal in winds, or (2) sustained north/easterly winds, with response mechanisms governed by ice conditions and interactions with the coastline.

Deleted: also

Deleted: the emergence of a shear-shock event (SSE) that results in reduced ice concentrations for triplets B, C, and D, one, three and five days following the SSE, respectively and loss of synchronicity in ice-atmosphere interactions

Deleted: .

Deleted: "shock-response" systems

1 Introduction

Central to our understanding of changes in the Arctic sea ice cover in response to a changing climate and continued anthropogenic forcing is an understanding of sea ice drift and deformation, namely sea ice dynamics. Accelerated ice drift speed over the past several decades reflects a weaker and more mobile ice cover associated with the loss of multiyear ice and changes in atmospheric circulation (Hakkinen et al. 2008; Barber et al., 2009; Rampal et al. 2009b; Spreen et al., 2011; Kwok et al., 2013). Sea ice deformation, or spatial gradients in the ice drift field, associated with opening and closing in the ice cover due to sea ice divergence and convergence, influences moisture and heat exchange between the ocean and atmosphere, ice ridging, sea ice thickness and redistribution (Hutchings et al., 2011, Bouillon et al., 2015) with implications ice hazard detection, and pollutant and contaminant transport. In the Beaufort Sea region, sea ice dynamics is governed by large-scale anticyclonic circulation of the Beaufort Gyre, with reversal to cyclonic circulation throughout the annual cycle (LeDrew et al. 1991; Preller and Posey, 1989; Proshutinsky et al., 2015).

When the ice cover on polar seas changes suddenly, navigation channels are altered as a result of ice-ice and ice-coastline momentum and energy flux exchanges (e.g., The Polar Group, 1980; Hwang, 2005; McPhee, 2012), air-sea heat exchanges increase (e.g., Carmack et al., 2015), and newly opened leads vent high moisture into the atmosphere as a strong mass exchange process (Bourassa et al., 2013). Understanding how these changes develop and relate to the orientation of a coastline is essential when diagnosing response patterns. For clarity, sudden change in this study refers to changes in the ice drift path relative to storm tracks, which have typical duration on the order of days and recurrence rates on the order of several days to weeks.

Deleted:

Arctic air-ice-sea interactions on synoptic timescales (several days to weeks) are governed by a force balance consisting of three interactive components: i) sea ice motion, ii) a confining coastline, and iii) atmospheric forcing. Previous studies have examined sea ice drift and deformation response to atmospheric forcing and coastline geometry on varying timescales (Overland et al., 1995; Richter-Menge et al., 2002; Geiger and Perovich, 2008; Hutchings et al., 2011). In an assessment of springtime sea ice drift in a region to the west of the Antarctic Peninsula, Geiger and Perovich (2008) identified low-frequency motion in response to atmospheric forcing and coastal geometry associated with

regional-scale transport, and higher-frequency near-inertial oscillatory motion associated with mixing. On regional and synoptic scales, Richter-Menge et al. (2002) also distinguish between translational and differential motion associated with shear zones and discontinuities in the ice drift characteristics in the southern Beaufort Sea.

The role of forcing (wind stress) and coastline geometry in establishing coherence in lead patterns/fractures in the ice cover captured by sea ice deformation has also been explored in past studies (Overland et al., 1995; Hutchings et al., 2005, 2011). Overland et al. (1995) demonstrated that in the Beaufort Sea for spatial scales: i) exceeding 100 km the sea ice cover moves as an aggregate; ii) less than 100 km the ice cover moves as an aggregate or discrete entity based on whether an elliptic (homogeneous) or hyperbolic (discrete) regime is established relative to the coastline (ice-coast interactions); and iii) on the order of 1 km the ice cover is characterized by floe (ice-ice) interactions. Through analysis of a nested beacon configuration and array with spatial scales ranging from 10 km to 140 km as part of the late winter (April) 2007 Sea Ice Experiment: Dynamic Nature of the Arctic (SEDNA) campaign in the Beaufort Sea, Hutchings et al. (2011) demonstrated coherence between 140 km and 20km divergence arrays for time periods of up to 16 days in March. Over shorter (sub-synoptic) timescales from May 2007 onward, nested buoy arrays captured the loss of connectivity in the sea ice cover associated with the winter-to-summer transition during a substantial ice-loss year (Stroeve et al., 2008).

In this study, we extend these analyses to quantify changes in the ice cover and in particular to explore sea ice drift and deformation using Lagrangian dispersion statistics. For simplicity and for the synoptic timescales considered in this study, we ignore lower-frequency ocean current fluctuations. We also ignore higher-frequency fluctuations associated with inertial oscillations, which are explored in a companion paper (Geiger and Lukovich, in preparation). We instead focus here on the spatiotemporal synoptic changes in sea ice drift and deformation that are directly related to storm tracks while they are developing and migrating through a local region, using a novel observational and analytical approach based on one-, two-, and three-particle dispersion analyses and evolution of beacons deployed in a triangular configuration as triplets

Deleted: in response to on-, off-, and along-shore winds based on distance from the coastline

Deleted: a

Deleted: i

Central to developing the tools required to understand sea ice drift and deformation in response to atmospheric forcing and ice-coastline interactions are diagnostics and in the case of drifting buoys, a Lagrangian framework to quantify spatiotemporal changes in the ice cover. Previous studies have used Lagrangian dispersion and ice beacon trajectories to quantify sea ice drift and deformation in the Arctic (Colony and Thorndike, 1984, 1985; Rampal, 2008, 2009a,b; Lukovich et al., 2011, 2014, 2015). Single-particle (absolute) dispersion provides a signature of large-scale circulation and captures linear time-dependence in fluctuating velocity variance characteristic of turbulent diffusion theory (Taylor, 1921; Rampal et al., 2009); i.e., departures in ice fluctuating velocity statistics from turbulent diffusion are attributed to intermittency associated with sea ice deformation and internal ice stress (Rampal et al., 2009).

A two-particle (relative) dispersion analysis monitors sea ice deformation. Through evaluation of buoy pair separations as a proxy of strain-rate (divergence, convergence, and strain) components combined, two-particle dispersion demonstrates heterogeneity and intermittency in the sea ice deformation field associated with space/time coupling inherent in fracturing of the sea ice cover as described by sea ice mechanics (Rampal et al., 2008; Weiss, 2013; Weiss and Dansereau, 2017). Rampal et al. (2008) noted that a triplet or multiple-particle analysis is in addition necessary to illustrate the deformation and related small-scale kinematic features that develop in sea ice.

Three -particle dispersion and triplet areas in particular, such as are explored in this study, enable a distinction between the individual strain-rate tensor components of divergence, convergence, and shear. Specifically, sea ice divergence depicts open water formation and accompanying processes such as new ice growth, brine rejection to the ocean, and heat and moisture exchange; ice convergence depicts ridge and keel formation thus contributing to ice thickness (Stern and Lindsay, 2009; Kwok and Cunningham, 2012), with implications for ice hazard detection, oil spill and contaminant transport and shipping route assessments. Triplet areas also provide a signature of what is referred to by Thorndike (1986) as "nondivergent diffusive mixing" due to compressibility in the ice cover.

Early studies of oceanic circulation have used multiple particles to monitor small-scale deformation and mixing as opposed to larger-scale stirring mechanisms captured by single-particle dispersion analyses. Ice beacon triplet arrays have also been used to monitor sea ice deformation off the Canadian

Deleted: an understanding of

Deleted: is the development of

east coast and in Antarctica (Prinsenberg et al., 1997; Heil et al., 2002; 2008; 2009; 2011). Studies of correspondence between ice stress, convergence and atmospheric forcing off the southern coast of Labrador in March, 1996 showed little change in convergence within an already compact ice cover, in addition to an increase in stress with winds and decrease in stress with temperature as the icepack loses its ability to transmit pressure (Prinsenberg et al., 1997). These results are consistent with studies of derived ice motion fields using synthetic aperture radar data showing sea ice deformation and production 1.5 times higher in the seasonal than in the perennial ice zone throughout the Arctic in late fall and winter due to differences in ice strength and thickness (Kwok, 2006).

Application of Lagrangian dispersion (single- and two-particle) in the seasonal ice zone in the Beaufort Sea region in past studies showed that single-particle dispersion captures the existence of two distinct dynamical regimes characterized by distinctive scaling laws; t^2 scaling in the zonal direction characteristic of advection, and $t^{5/4}$ scaling in the meridional direction characteristic of quasi-geostrophic 2D turbulence (Lukovich et al., 2011). Two-particle dispersion studies in this region, based on an assessment of loop and meander reversal events, demonstrated enhanced meridional separation indicative of ice-ice and ice-coast interactions and increased connectivity in the ice cover in winter relative to spring (Lukovich et al., 2014).

In the present study we build upon these previous analyses to provide, using one-, two-, and three-particle dispersion analyses, a prescription for changes in sea ice drift trajectories and deformation in response to atmospheric forcing and coastal interactions for varying distances from the coastline. In particular, we seek to address the following research questions:

i) What is the correspondence between sudden changes in sea ice drift trajectories, atmospheric forcing, and distance relative to the coastline on daily timescales? [How can individual sea ice drift events be characterized?]

ii) How are sudden changes manifested in deformation characteristics? How do these characteristics vary daily based on orientation (near shore, offshore, and along shore) and distance relative to the coast?

The goal of this paper is to develop a framework for understanding sudden changes in ice drift trajectories in the Beaufort Sea on daily timescales using Lagrangian dispersion statistics to quantify

Deleted: and more generally synoptic

Deleted: and synoptic

Deleted: triplet centroids and areas

drift and deformation relevant both from an observational and modelling perspective, with the potential for application to an assessment of dynamical regimes in other regions of the Arctic.

The paper proceeds as follows. Data used to identify sudden changes in sea ice drift are described in Section 2. In Section 3, methods based on Lagrangian dispersion and the triplet area approach, are presented. Results associated with each of the two objectives are provided in Section 4, followed by a summary of results in Section 6 in addition to a short description of future work.

Deleted: , respectively,

Deleted: three-particle

Deleted: discussions of results in the context of sudden changes in Section 5, and

Deleted: conclusions

2 Data

Sea ice position data were obtained from an array of ten ice beacons and one ice mass balance buoy launched from the CCGS *Amundsen* in the marginal ice zone of the southern Beaufort Sea in September, 2009 (Figure 1). From this array, four triangular configurations were selected, hereinafter referred to as triplets A to D, to monitor divergence and convergence of sea ice, with initial inter-beacon distances of approximately 11, 11, 11.5, and 7 km for the shortest leg, and 15, 37, 11.5, and 12.5 km for the longest leg, respectively. Triplets A to D were deployed on multi-year ice (MYI) and labeled according to their proximity to the continental coastline: triplet A was located closest to the coastline, while triplet D was located furthest from the coastline. Position coordinates were available for all beacons in: triplet A until October 6th; triplet B until November 4th; triplet C until November 25th, and triplet D until November 3rd, yielding time intervals with durations of 28, 56, 77, and 59 days, respectively. As reported in Lukovich et al. (2011), positional accuracy of the ice beacons ranged from $\delta x = 2.5$ to 5 m based on circular and spherical error probability associated with the GPS module, while temporal accuracy was on the order of nanoseconds and thus negligible. Position accuracy for the ice mass balance buoys was less than 3m according to Garmin GPS16X-HVS product Standard GPS accuracy. The temporal resolution of the beacon data is two hours, and daily averages were calculated for the analysis and time series. Since the anticipated lifetime of the beacon batteries is at least one year, the beacon longevity may be attributed either to alternative mechanical failure or ice deformation and ridging. The data are archived long term through the Canadian Polar Data Catalogue (Buoy triplet centroid 2009 data, 2016).

Deleted: and Table I

Sea ice extent and ice type are examined using Environment Canada Canadian Ice Service (CIS) weekly ice charts, in addition to 12.5 km resolution Advanced Microwave Scanning Radiometer – EOS (AMSR-E) daily sea ice concentration (SIC) data. Daily and weekly maps illustrate spatial variability of sea ice concentrations in the Beaufort Sea, while also enabling an assessment of ice conditions in the vicinity of the triplet centroids during their evolution from September to November, 2009.

Atmospheric forcing in the form of sea level pressure (SLP), wind speed and direction, and surface air temperature (SAT) was obtained from North American Regional Reanalysis (NARR) data (Mesinger et al., 2006). Daily atmospheric forcing is derived by averaging 3-hourly NARR data in the vicinity of triplet centroids. Time series of daily-averaged sea level pressure (SLP) are then characterized into relative high (maxima) and low (minima) pressure tendencies. Time series of daily-averaged 10m NARR winds are used to characterize on-shore and off-shore winds.

3 Methods

In this section we describe the Lagrangian dispersion and triplet centroid approach used to quantify i) sudden changes in ice drift trajectories and ii) corresponding sea ice deformation that develops in response to atmospheric forcing for varying distances from the coastline. Presented also are diagnostics (base-to-height and perimeter-to-area ratios, Okubo-Weiss criterion, and shear-to-divergence ratios) used to characterize sea ice drift and deformation during sudden changes in ice drift paths.

3.1 Single-particle dispersion, triplet centroids, and sudden changes in ice drift trajectories

Single-particle dispersion monitors organized structure in the flow field and is defined as (Taylor, 1921)

$$A^2 = \langle |x_i(t) - x_i(0) - \langle x_i(t) - x_i(0) \rangle|^2 \rangle$$

for x_i the zonal and meridional location of the ith particle/beacon in the ensemble as a function of elapsed time, t, and where angle brackets denote ensemble averaging. Flow dynamics are characterized by the scaling exponent α according to the relation

$$A^2 \sim t^{\alpha},$$

Deleted: methods used to compute

Deleted: triplet centroids and

Deleted: triplet areas and sea ice deformation

Deleted: and interaction

Deleted: s

Deleted: with

Deleted: As is further described below, 'shock' parameters used to evaluate sudden changes in ice drift include SLP and turning angles, SAT and SIC in the vicinity of triplet centroids, in addition to NARR winds, ice drift and orientation. Each of these techniques is used to quantify sea ice drift in response to atmospheric forcing and ice-coast interactions. 'Response' parameters and diagnostics used to evaluate manifestation of sudden changes in deformation include triplet area, perimeter-to-area ratios, the Okubo-Weiss criterion, and the shear-to-divergence ratio.

Deleted: Sudden changes in ice drift trajectories

Formatted: Font:Italic

Formatted: Right: -0.09 cm

where $\alpha = 2$ corresponds to a ballistic regime indicative of advection, $\alpha = 1$ to a diffusive regime, $\alpha = 5/3$ to an elliptic regime, $\alpha = 5/4$ to a hyperbolic regime, and $\alpha < 1$ to a subdiffusive or "trapping" regime. As noted in previous studies, in the context of sea ice dynamics, a ballistic dispersion regime depicts advection associated with organized structure in the ice drift field, while a diffusive regime captures the behaviour of particles/beacons/ice floes that follow independent random walks (Provenzale, 1999). A subdiffusive regime characterizes trapping such as would occur with dominant contributions from ice-ice-interactions. An elliptic regime indicates a strong rotational component in the ice drift field, whereas a hyperbolic regime indicates strain (shear and stretching)-dominated flow associated with along-shear transport such as, in this study region, anticyclonic Beaufort Gyre circulation. Previous studies have illustrated the use of Lagrangian dispersion statistics to quantify dynamical regimes in the ice cover (Rampal et al., 2009a,b; Lukovich et al., 2011, 2015; Rampal et al., 2016). In this study, we build upon previous analyses by identifying inflection points in total absolute dispersion results to identify transitions in distinct dynamical regimes.

Triplet centroids are calculated from the latitude/longitude coordinates of the three beacons comprising triplets A to D. Sudden changes in triplet centroid trajectories on daily timescales are calculated by applying a three-day running mean to centroid positions, and computing the variance after each mean calculation. The total variance is calculated as the square root of the sum of the squared latitudinal and longitudinal variances. Sudden changes are identified according to minima in the total variance time series, capturing interruptions to the ice drift path.

Ice and atmospheric conditions are investigated according to the spatial and temporal evolution in ice beacon triplet centroids. Ice drift velocities for each triplet centroid, computed as outlined in Appendix A, further highlight acceleration/deceleration in the triplets during fall, 2009. Turning angles are calculated as the difference between 10 m NARR surface winds and beacon-derived ice drift.

3.2 Two- and three-particle dispersion and sea ice deformation

Two-particle dispersion monitors the separation in a pair of particles/beacons/ice floes and is defined as

$$R^2 = \langle (x_i(t) - x_{i+1}(t) - \langle x_i - x_{i+1} \rangle)^2 \rangle$$

Deleted: or "shocks"

Deleted: The term "shocks" is used interchangeably with sudden change from the perspective of a 'shock-response' mechanism associated with sea ice response to atmospheric forcing and ice-coast interactions on daily timescales that forms the focus for the present study.

Deleted: Lagrangian dispersion

for adjacent particle pairs x_i and x_{i+1}, and where angle brackets again denote ensemble averaging. In contrast to single-particle dispersion, two-particle dispersion reflects the behaviour of spatial gradients in the ice drift field rather than the ice drift field itself. Dynamical regimes associated with velocity gradients are defined according to the relation $R^2 \sim t^\beta$. In short- and long-time limits, particles experience linear displacements and approach behaviour comparable to single particles as the pairs lose memory of their origin, respectively. For intermediate times, $R^2 \sim t^3$, in what is referred to as Richardson's (1926) law, resulting from the assumption that eddy diffusivities are dependent on inter-particle separation. In the context of sea ice dynamics, two-particle dispersion characterizes intermittency and heterogeneity in the ice drift field.

In consideration of three-particle dispersion, triplet areas were computed from recorded beacon latitude/longitude coordinates using Heron's formula $A = \sqrt{s(s-a)(s-b)(s-c)}$, where a, b, and c denote the length of the sides for each triplet, and $s = \frac{1}{2}(a+b+c)$. Error propagation analysis for the triangle area and triplet evolution according to Heron's formula yields initial error estimates on the order of $\delta_A = \frac{\delta x}{\sqrt{8}A}\sqrt{(b^2+c^2-a^2)^2a^2 + (a^2+c^2-b^2)^2b^2 + (a^2+b^2-c^2)^2c^2} \sim 0.05$, 0.12, 0.04, and 0.04 km^2 for triplets A to D, respectively.

An assessment of the time rate of change in triplet area provides insight about sea ice deformation, namely the differential kinematic parameters (DKPs) of divergence (D), vorticity (V), shearing (S) and stretching (N) deformation rates. In particular, the change in area of a triangular configuration or triplet of drifters to estimate the divergence and local change in flow can be expressed as

$$D = \frac{1}{A}\frac{dA}{dt} = \frac{\partial u}{\partial x} + \frac{\partial v}{\partial y},$$

where A denotes the triangle area, and u and v depict the zonal and meridional components of ocean circulation or ice drift (following Molinari and Kirwan, 1975; LaCasce, 2008; Wadhams, 1989) with negative values corresponding to convergence. Similarly gradients in sea ice motion or deformation characteristics such as vorticity, shearing and stretching deformation rates can be computed from changes in the triplet area through rotation of the velocity vectors (Saucier, 1955). Comparable expressions and their relations are provided both from an oceanic perspective (Saucier, 1955; Molinari

Formatted: Indent: First line: 0.7 cm

Deleted: T

and Kirwan, 1975), and in an assessment of sea ice deformation in the Weddell Sea in Wadhams (1989) such that:

$$V = \frac{\partial v}{\partial x} - \frac{\partial u}{\partial y} = \frac{1}{A'}\frac{dA'}{dt}; u' = v \; and \; v' = -u$$

$$S = \frac{\partial u}{\partial y} + \frac{\partial v}{\partial x} = \frac{1}{A''}\frac{dA''}{dt}; u'' = v \; and \; v'' = u$$

$$N = \frac{\partial u}{\partial x} - \frac{\partial v}{\partial y} = \frac{1}{A'''}\frac{dA'''}{dt}; u''' = u \; and \; v''' = -v$$

where primes indicate 90° clockwise rotation of velocity vectors. Divergence is associated with a change in area, vorticity with a change in orientation, and shear and stretching with a change in triangle shape due to distortion (Table 2). According to the error estimates for triplet area, a threshold value for significant DKPs relative to uncertainties to ensure a sufficiently large signal to noise ratio is on the order of 10^{-6} s^{-1} for the daily timescales considered.

From the perspective of physical changes in sea ice, divergence (convergence) captures opening (closing) in the ice cover related to ice-ocean interactions and flux exchange (ridging). In the Arctic, negative (positive) vorticity depicts anticyclonic (cyclonic) circulation associated with surface winds and inertial oscillations. Negative (positive) shear captures a shape change whereby the northern triangle beacons travel west (east) relative to the southern pair without changing the triangle area. A negative stretching deformation rate (hereinafter referred to as stretching) indicates stretching along the y-axis (north-south), and shrinking along the x-axis (east-west), without changing the triangle orientation (i.e. stretching parallel or perpendicular to the coast).

In non-divergent flow, the triplet area is conserved so that expansion in one direction is accompanied by contraction in another direction and the triangle becomes an elongated filament (Prinsenberg et al., 1998). Changes in the aspect ratio (defined as the longest leg, or base, divided by the height) also describe changes in the triplet area; i.e., increasing values indicate elongation of the triplet and filamentation or stretching of the triangular configuration, while decreasing values indicate an equilateral configuration. An equilateral triangle is depicted by a base-to-height ratio of $\frac{2}{\sqrt{3}} \sim 1.155$. Furthermore, the perimeter-to-area ratio provides a signature of 'folding' in the sea ice drift cover in a manner similar to mechanical annealing whereby compression reduces the dislocation density of

Formatted: Indent: Left: 0 cm, First line: 0.7 cm

materials (Shan et al., 2007; Lawrence Berkeley National Laboratory, 2008). Perimeter-to-area ratios may also provide insight about floe shape and size distributions (Gherardi and Lagomarsino, 2015). Elongated triangles are captured by vanishing perimeter-to-area ratios, while an equilateral configuration is depicted by a perimeter-to-area ratio of ~$4\sqrt{3}/a$, where a is the length of the equilateral triangle side.

Previous studies of DKPs using the triangle area approach have shown that the role of triplet areas in describing DKPs resides in the evolution in the time rate of change in the triangle area (Saucier, 1955; Molinari and Kirwan, 1975). If the lengths of the base (defined as the longest triangle side) and height (defined as the perpendicular distance and 2A/b) differ by an order of magnitude so that the triangle is significantly distorted, a decrease in area will occur. If in addition the change in area exceeds its uncertainty, the DKP associated with the relevant rotation of coordinates will increase, providing a signature of strong deformation. If, however, little change in triplet area is observed (less than the area uncertainty ~ 0.12 km^2), the DKP in question will essentially vanish. In the present study, as is noted below, minimum values for the triplet area amongst all triplets are on the order of 10 km.

Relative contributions of the DKPs are monitored using total deformation $D^2+S^2+N^2$ to assess distortion in the ice cover due to divergence, and the shearing and stretching deformation rates, as well as the vorticity squared V^2 to assess the rotational component (capturing influence from winds and/or inertial oscillations (Gimbert et al, 2012, albeit on shorter timescales)). The Okubo-Weiss (OW) criterion, defined as (Okubo, 1970; Weiss, 1991)

$$OW = Re\left(\frac{1}{4}\left(D^2 + S^2 + N^2 - V^2 + |D|\sqrt{S^2 + N^2 - V^2}\right)\right),$$

highlights relative contributions from deformation and the rotational component. Values with OW < 0 (OW > 0) indicate flow dominated by vorticity (deformation). In order to further distinguish relative contributions from divergence, shearing and stretching deformation rates to the total deformation, the shear to divergence ratio is evaluated such that

$$\theta = arctan\left(\frac{\sqrt{S^2 + N^2}}{D}\right),$$

Deleted:

Formatted: Superscript

Deleted: the diagnostics of

as a signature of sea ice stress, with implications for rheological characterizations. The shear-to-divergence ratio demonstrates spatial and temporal variability in DKPs and rheological characterizations of the sea ice cover. Values of 0, 45, 90, 135, and 180 degrees depict divergence, extension, shear, contraction, and convergence, respectively (Feltham, 2008; Fossen, 2016).

4 Results and discussion

In this section, we identify sudden changes in sea ice drift and corresponding sea ice deformation characteristics using Lagrangian dispersion statistics and additional diagnostics in the context of triplets A to D based on distance from the coastline. Specifically, in the first subsection, single-particle dispersion and factors contributing to identified changes in sea ice drift and dynamical regimes including SLP, surface winds, SAT and sea ice conditions in the vicinity of triplets A to D are investigated. In the second subsection, sea ice deformation is examined using two- and three-particle dispersion statistics.

4.1 Single-particle dispersion and identifying sudden changes in sea ice drift

Figure 1. Evolution in Triplet A to D centroid trajectories.

Trajectories for beacons deployed near 135 °W between 72 °N and 75 °N capture spatiotemporal evolution in ice beacon triplet centroids beginning in September, 2009, with triplet A located closest to, and triplet D located furthest from, the continental coastline (Figure 1). Triplets A and B, deployed near 72 °N, share two of the three beacons and are advected westwards to approximately 144 °W and 158 °W, surviving until October 7th and November 5th, respectively. Triplet C is deployed near 73 °N and is also advected westward to 162 °W, surviving until November 26th. Triplet D is deployed near 74.5 °N and traverses a shorter path southwards and westwards to 145 °W, surviving until November 4th.

From September to November, 2009, eight sudden (local) change events are identified based on changes in the (regional-scale) ice drift path (Figure 1 and Table 1). An initial sudden change event *e1* depicts a cusp in all centroid trajectories; a second event *e2* depicts southwestward advection in triplets A to C and delayed southward migration in Triplet D; a third event *e3* captures southward migration for

Deleted: Sought in this study is a cumulative assessment and narrative that describes relative contributions of deformation and vorticity using concepts from Lagrangian dispersion and three-particle dispersion in particular, rather than a comparison between different techniques. The quality of this approach is determined by consistency of results using each method that contribute to an overall account of spatiotemporal changes in sea ice drift and deformation on daily timescales.

Deleted: , and responses as manifested in sea ice deformation using shock-response diagnostics

Deleted: shock parameters including

Deleted: sea ice responses to atmospheric forcing and ice-coastline interactions are examined in the context of triplet areas, sea ice deformation, relative sea ice deformation (i.e. deformation- or vorticity-dominated flow), and shear-to-divergence ratios. A detailed description of results is provided in the triplet observation report in Appendix B.

Deleted: I

Deleted: s or "shocks"

Deleted: change

Deleted: shock

Deleted: shock

all four triplet centroids; *e4* the onset of south and westward migration; *e5* the onset of south and northwestward migration for all triplet centroids culminating in a loop event for Triplet D centroid trajectories and following which triplet A stops recording (October 6th); *e6* depicts northwestward migration in triplets B and C, and a cusp in triplet D; *e7* northwestward migration for all triplet centroid trajectories; *e8* captures northwestward migration and a loop in triplet C and D centroid trajectories (Figure 1 and Table 1).

Figure 2. Sudden changes in Triplet A to D centroid trajectories

Sudden changes in triplet centroid trajectories on daily timescales are, as previously noted, quantified by time series for total variances of the 3-day running mean triplet centroid positions, and identified according to minima in these time series (Figure 2). Enhanced latitudinal variance is observed for Triplet D relative to Triplet A in late September/early October. By contrast longitudinal variance decreases with increasing distance from the coastline, evidenced in lower values for triplet D relative to triplet A.

Minima in the total variances of the 3-day running mean triplet centroid positions capture sudden changes and interruptions in the ice drift field. Maxima also capture departures from the ice drift path. Comparison of SLP highs (Figure 5) and maxima in centroid position variances (Figure 2) demonstrates correspondence between both prior to 8 October during what is described below as the SLP high resulting in Ekman convergence, strong off-shore ice drift, and deterioration in the ice cover. Similar behavior is observed in mean SLP and ice drift triplet centroid variances for all triplets until 8 October, following which SLP and centroid variance maxima are out of phase with a lag of approximately two days.

Figure 3. – Absolute (single-particle) dispersion for all triplets, and regional characterization of sea ice drift.

Deleted: a (shocks)

Deleted: or "shocks"

Deleted: Noteworthy is e

Deleted: Successive minima for triplets C and D in *e1* indicate a sustained response to external forcing; 1 – 2-day lagged responses in triplets C and D centroids for *e2* – *e4* indicate delayed responses to external forcing and highlight an absence of temporal coherence between triplet centroids. Following mid-October, shocks associated with triplets C and D coincide with or precede triplet B responses at lower latitudes.

Deleted: . ... [1]

Deleted: .

Deleted: 3

Deleted: and

Deleted: as the shear shock event (SSE)

Deleted: A loss of spatial and temporal synchronicity in triplet B to D variance values is further observed following the SSE event.

The loss of synchronicity ocean-sea ice-atmosphere interactions is further demonstrated in single-particle dispersion statistics for an ensemble including all triplets, providing a regional characterization of sea ice drift in the Southern Beaufort Seas (Figure 3). Specifically, total absolute dispersion is governed by zonal dispersion prior to, and meridional dispersion following, early October, with scaling exponents of $\alpha \sim 3$ and 2, respectively, highlighting a transition in dynamical regimes. Sudden change events captured by the (Eulerian) variance interpretation (Figure 2) are also captured by inflection points in the (Lagrangian) single-particle, and most notably, meridional, dispersion analyses (Figure 3).

Figure 4. – Absolute dispersion for beacons comprising triplets, and a local characterization of sea ice drift.

An assessment of local sea ice drift characteristics using single-particle dispersion and a three-beacon ensemble for each centroid demonstrates regional differences in the ice cover for varying distances from the coastline (Figures 4a and 4b). Triplets A and B, located closest to the coastline, exhibit considerable meridional variability relative to triplets C and D (upper panel in Figure 4a). Single-particle displacements are also shown to decrease with increasing distance from the coastline. Total absolute dispersion is governed by zonal dispersion (Figure 4a). Furthermore, inflection points in absolute dispersion associated with the local characterization (Figure 4) capture transitions in dynamical regimes due to changes in local ice conditions.

Triplets A and B are characterized by sub-diffusive ($\alpha < 1$) behaviour from 19 September, 2009 to 6 October, 2009, and from 17 – 21, October, 2009, and super-diffusive ($\alpha > 2$) scaling from 7 – 12 October, 2009, and following 22nd October (Figure 4b). Triplet C, located further from the coastline, experiences similar sub-diffusive behaviour prior to 6 October, 2009, and predominantly super-diffusive behaviour following 12 October, 2009. Triplet D, located furthest from the continental coastline experiences the smallest displacements between beacons, with sub-diffusive scaling to 5 October, 2009, and diffusive scaling following 19 October, 2009, with no instances of ballistic scaling. As is explored further below, these dynamical regimes correspond to changes in atmospheric and sea ice conditions.

Deleted:

Formatted: Indent: First line: 0.7 cm

Formatted: Superscript

Figure 5 – Atmospheric forcing and sea ice response – spatial variability

Investigation of atmospheric and sea ice conditions (Figures 5 to 7) shows that mean SLP in the vicinity of triplets A to D is uniform, with some differences in the vicinity of triplet D (Figure 5). By contrast, turning angles highlight spatial variability in ice drift for intervals between high SLP regimes, and provide an initial indication of sea ice mechanics and deformation. Specifically, differences in turning angles highlight spatial (relative to distance from the coastline) differences in sea ice response to external forcing as the SLP high enters the region in the vicinity of the beacon triplets on 8 October, 2009, and subsequent loss of coherence in the ice cover.

Figure 6 – NARR winds, sea ice drift and orientation – spatial variability

Winds and ice drift show coherence in ice drift for triplets A to C, and variations in triplet D (Figure 6). Orientation highlights increased free drift conditions at higher latitudes associated with triplet D relative to lower latitude triplets. Sudden changes in sea ice drift occur between SLP high regimes (Figures 2, 3, 5 and 6 and Table 1). In particular, events *e1*, *e3*, *e4*, *e6* and *e8* occur during reversals in wind and ice drift (Figure 6). Noteworthy also are sudden changes in sea ice drift during persistent (~ 3 – 4 days) northerly winds (events *e2*, *e5* and *e7* in Figure 2 and Table 1). Of particular interest is strong offshore ice drift on 8 October due to easterly winds and strong Ekman convergence during a SLP high within a high ice concentration (> 95%) ice regime.

Figure 7 – SIC range and SAT – spatial variability

Surface air temperature (SAT) and sea ice concentrations (SIC) in the vicinity of triplet centroids show that SAT values less than 2 ºC are sustained following 14 September, 2009 for triplets A to D, with an interval of increased SAT near 14 October (Figure 7). SIC varies for triplets A to D, with lower concentrations to 24 September. Low SIC exists during a SLP high for triplet C near 22 September. Lower SICs are observed following the 8 October SLP high indicating deterioration in the sea ice cover.

Deleted: 3

Deleted: M

Deleted: 3

Deleted: .

Deleted: Positive turning angles correspond to increasing mean SLP and negative turning angles to decreasing SLP for all but triplet D. In contrast to SLP, turning angles provide a regional characterization of differences in sea ice drift response based on distance from the coastline ... [2]

Deleted: 4

Deleted:

Formatted: Indent: First line: 0 cm

Deleted: ... [3]

Deleted: 5

Deleted: 5

Deleted: exists during a SLP low for triplet D during the first loop event in mid-October.

Figure 8 – Sea ice conditions prior to, during, and following the 8 October SLP high.

An assessment of sea ice and atmospheric conditions shows that the transition in dynamical regimes depicted in the variance time series and absolute dispersion in particular (Figure 3) occurs during a SLP maximum/high, accompanying Ekman convergence and offshore drift. This is further reflected in the poleward retreat in the sea ice edge on 9 and 10 October (Figure 8). In addition, the increase and decrease in meridional displacements during the SLP high for triplets A to D (Figure 3) reflect offshore Ekman drift within a high concentration regime (that suppresses meridional displacements) and subsequent increase in meridional displacements two days following within lower ice concentration regimes indicating failure in the ice cover (Figures 3 and 8). Local ice drift conditions are reflected in subdiffusive scaling (α <1) in total dispersion indicating limited displacements for triplet B within a high ice concentration regime relative to triplets C and D, where beacons exist within lower ice concentration regimes (Figures 4 and 8) near 19 October.

In summary, results from this section show that single-particle dispersion (namely inflection points in meridional single-particle dispersion statistics) captures sudden changes evident in ice drift paths and minima in centroid drift variance, and provides a regional characterization of sea ice drift. Local differences in ice drift are manifested in absolute dispersion for beacons associated with each triplet. Moreover, absolute dispersion demonstrates a shift in sea ice dynamics during the SLP high on 8 October responsible for convergence in the ice cover, poleward retreat in the ice edge, and strong offshore ice drift.

Formatted: Indent: First line: 1.27 cm

Deleted: Lower SIC also exists for triplet B as it approaches the ice edge in November (not shown).

Deleted: Identifying responses in

4.2 Two- and three-particle dispersion and sea ice deformation

Figure 9. Relative (two-particle dispersion).

Moved down [1]: Figure 6 Triplet area evolution

In this section we explore sea ice drift, and deformation in particular, in the context of two- and three-particle dispersion based on distance relative to the coastline. Relative (two-particle) dispersion shows that total dispersion is initially governed by zonal separation for triplets A, B, and C, and by both zonal

and meridional separation for triplet D (Figure 9). This distinction may be attributed to predominantly meridional motion (and along-shear transport) of triplet D along the eastern segment of the anticyclonic Beaufort Gyre. A significant decrease in zonal separation is observed near the ice edge in triplet B due to convergence in the ice cover in response to the SLP high. Inter-beacon distances also increase in the meridional direction and decrease in the zonal direction for triplet B following the SLP high on 8 October. A transition to a more isotropic state in the ice cover for triplets closest to the coastline is evident in comparable zonal and meridional separations in triplets B and C in particular (right panel in Figure 9) following October 27 as beacons encounter lower ice concentrations (Figures 7 and 9).

Whereas events e1, e3, e4, e6, and e8 are associated with reversals in surface winds, changes in along- and cross-shear separation accompany northerly winds during events e2, e5, e7, with delayed responses following the SLP high on 8 October. During e2, an increase in along-shear transport is observed for all triplets, with an increase in zonal separations for triplets A, B, and C in the direction of transport along the southern portion of the anticyclonic Beaufort Gyre, and in meridional separations for triplet D in the direction of motion along the eastern segment of the BG. During e5, an onset in an increase in across-shear transport, namely meridional separation, accompanied by a decrease in zonal separation is observed for triplet B, which is sustained during the SLP high. Following e7, a delayed increase in along-shear transport and zonal separation for all triplets is observed, providing further evidence of loss of synchronicity in ice-atmosphere interactions following the 8 October SLP high. Furthermore, t^3 scaling associated with Richardson's scaling law and attributed to atmospheric dispersion as described in Rampal et al. (2009), is evident ($\beta \sim 3.4$) for triplet C from 10 – 17 October; higher scaling exponents exist for triplets B and D following the SLP high on 8 October.

Formatted: Font:Italic

Formatted: Font:Italic, Superscript

Figure 10. Triplet area evolution

Moved (insertion) [1]

Deleted: 6

Figure 11. Evolution in triplet area, base, height, and aspect ratios.

Regional differences in triplet area representative of sea ice deformation are observed in the evolution of all triplet triangles (Figure 10). Specifically, triplet area evolution demonstrates enhanced variability in triplet B relative to triplets A, C, and D, with an increase in area near the ice edge in late October/early November (Figure 11). An increase in triangle base (defined as the longest triangle side) is observed with decreasing distance from the coastline (i.e. higher base values for triplets A and B relative to triplets C and D), in a manner consistent with local absolute dispersion (Figure 4). The triplet base also provides a measure of two-particle dispersion and separation between a pair of particles/beacons/ice floes. Triplet area is governed by height. Base-to-height and perimeter to area ratios illustrate an equilateral configuration near the ice edge and coastline in the early stages of evolution for triplet A, and late stages of evolution for triplet B, captured in base-to-height ratio values approaching 1.155. Stretching is observed closest to the coastline following 10 October during a consolidated ice regime (Triplet B), captured in increasing perimeter-to-area and base-to-height ratios.

As for two-particle dispersion, changes in area, height, and P/A and b/h ratios capture deformation associated with events e2, e5, and e7, with delayed responses to northerly winds following the 8 October SLP high (Figure 11). Following *e2*, the base for triplets A and B increases and height decreases during consolidation, resulting in enhanced P/A and b/h. By contrast, P/A and b/h are approximately constant for triplets C and D, indicating that the triangle maintains its shape further from the continental coastline. Following e5 and the SLP high, the greatest stretching (high base and ratio values) is observed in triplet B located closest to the coastline. Several days following *e7* a decrease in area for triplet B is associated with an decrease in height so that b/h and P/A increase, while once again the area and ratios for triplet C and D remain constant.

Also of interest is enhanced variability in height and area indicating divergence/convergence closer to the coastline, namely for triplet B, following the 8 October SLP high. Triplet C experiences a sustained increase in the triangle base, height, and area following 8 October, in a manner consistent with Gulf of Mexico drifters as described by LaCasce (2008). Referring to a drifter study by LaCasce and Ohlmann (2003), LaCasce (2008) indicated that a sustained increase in triangle area provides a signature of a diffusive regime (such as surface winds) superimposed on ocean dynamics. Triplet D located furthest from the coastline experiences a weak and sustained increase in triangle height and

Deleted: dynamical (particularly deformation) responses to atmospheric forcing based on distance and orientation relative to the coastline.

Deleted: D

Deleted: 6a

Deleted: 6b

Formatted: Indent: First line: 0.7 cm

corresponding decrease in aspect ratio. P/A and b/h thus provide a signature of stretching, the relative contributions of which are further described by deformation and DKPs.

Figure 12, Sea ice deformation

Local differences in sea ice deformation are further reflected in differential kinematic parameters (DKPs) defined as the weighted time rate of change in triplet area, as described in the methods section (Figure 12). For triplet A, located closest to the coastline, sea ice deformation is characterized predominantly by vorticity and stretching (Figure 12). Triplet B is governed by vorticity for the duration of this triplet evolution, with contributions from shear until 8-10 October, and divergence and stretching following mid-October. Triplet C, located further from the coastline is characterized by vorticity in the early and late stages of triplet evolution with intermittent contributions from shear and to a lesser extent divergence during low ice concentration regimes. Triplet C also experiences enhanced vorticity following the 8 October SLP high. A strong shear event is in addition observed for triplet B during the SLP high on 8 October, and for triplet C on 10 October. Located furthest from the coastline, triplet D is governed by vorticity, stretching, shear, and divergence in the early stages of development, and by vorticity and to a lesser extent shear for the duration of the triplet evolution. Results further show that sea ice deformation is smallest furthest from the coastline.

In consideration of sudden changes due to northerly winds e2, e5, and e7, during *e2*, Triplet B experiences a transition from vorticity and stretching to shear, while triplet C is governed by shear. DKPs for triplets A and D are comparatively weak. Similarly during *e5*, weak DKPs are observed for triplet C, with triplets B and D governed by vorticity. During *e7* convergence and divergence dominate for triplet B.

Figure 14, Relative sea ice deformation.

Relative DKPs highlight relative contributions from external forcing associated with winds and bathymetry/distance from the coastline as manifested in vorticity and total deformation, namely the sum

Deleted: ... [4]
Formatted: Indent: First line: 0 cm
Deleted: 7
Deleted: The time rate of change in triplet area depicts sea ice drift response relative to the coastline.
Deleted: 7
Deleted: 10
Formatted: Indent: First line: 0.7 cm
Deleted: 8

of divergence, shear and stretching deformation rates squared. Results show reduced total deformation with increasing distance from the coastline (top panel, Figure 14), particularly following the SLP high on 8 October. Enhanced vorticity is also observed during low ice concentration regimes, as demonstrated in comparatively high values for triplet D in September, and for triplet B in late October/early November. The Okubo-Weiss criterion provides a signature of deformation- (OW > 0) and vorticity (OW < 0)-dominated regimes. Intervals of divergence and deformation-dominated flow prevail for triplet B, with some instances observed for triplet A, C, and D again in the early stages of evolution. The Okubo-Weiss criterion results in particular show enhanced distortion in the (bounded) ice cover closest to the coastline, especially following the 8 October SLP maximum. Theta values illustrate changes in the ice strength due to relative contributions from divergence and the total strain rate ($S^2 + N^2$). Noteworthy are the high (~180) values during e2, e7, and following e5, indicating convergence associated with offshore ice drift due to Ekman convergence and sea ice deformation associated with along- and across-shear transport.

Previous studies have demonstrated correspondence between ice deformation and stress measurements in the Beaufort Sea (Richter-Menge et al., 2002). Sea ice strength is dependent on ice concentration and thickness. The ice cover fails when the internal ice stress is comparable to ice strength. Results from this analysis suggest that the three-particle dispersion approach, and shear-to-divergence ratio as a measure of ice stress can be used, in combination with ice concentrations and thickness conditions to assess conditions for which failure in the ice cover occurs (Figures 7 and 14). Strong convergence (theta ~ 180) experienced by triplet C on 26 September within a high ice concentration regime, and subsequent reduction in SIC encountered by triplet beacons suggests local failure in the ice cover. In addition, compression experienced by triplet B during the 8 October SLP high and Ekman convergence coincides with reduced ice concentrations and the strong ice shear event (Figures 7, 12, and 14), also indicating failure in the ice cover with non-local effects on triplets C and D. This deterioration further continues near the ice edge for triplet B to 20 October as shear-to-divergence values on order of 180 are accompanied by significant reductions in ice concentrations as the triplet encounters the ice edge and free drift conditions. These results also suggest that sudden change events e2 and e7, associated with along-shear transport, northerly surface winds and ice deformation anticipate

Deleted: 8

Deleted:

Deleted: evident in higher values for triplet A in late September that accompany a decrease in SIC, and for triplet B in October and November relative to triplets C and D

Deleted: Noteworthy is the existence of vorticity-dominated flow for all triplets in the early stages of development.

Deleted: particularly following the shear shock event (SSE)

Deleted: and disintegration in the ice cover following the strong shear event, opening in the flaw lead (evident in reduced concentrations and increasing SAT in Figure 5) releasing heat to the atmosphere and resulting in increased SAT

Deleted: , as is discussed further below in Section 5 in the context of a prescription for identifying and describing 'shock-response' pairs

Formatted: Indent: First line: 1.27 cm, Widow/Orphan control, Adjust space between Latin and Asian text, Adjust space between Asian text and numbers

failure in the ice cover closest to the coastline, although additional study is required to confirm this hypothesis.

Figure 15. Scatter plots of NARR and DKPs: sudden changes in response to surface winds and DKPs.

An evaluation of scatter plots showing the number of triplet centroid values in the vicinity of NARR surface winds and associated DKPS highlights sea ice deformation characteristics based on distance from the coastline (Figure 15). Specifically, triplet B is characterized by strong deformation even for low wind speeds, and divergence following the SLP high, indicating dominant contributions from ice-ice interactions closest to the coastline. Deformation for triplet C is accompanied by surface winds on the order of 2 – 5 m/s; events are confined to or characterized by weak divergence and are governed primarily by shear. Triplet D located furthest from the coastline is characterized by shear at low wind speeds. Most events are associated with weak divergence, negative vorticity, and shear.

In summary, results from this section show that two- and three-particle dispersion capture sea ice deformation associated with sudden changes in ice drift paths in response to atmospheric forcing, for varying distances relative to the coastline. Specifically, two- and three-particle dispersion describe sea ice deformation induced by persistent northerly winds (events e2, e5, and e7), enhanced deformation and deterioration in the ice cover following the 8 October SLP high, and regional variations in sea ice deformation, with implications for rheological characterizations of sea ice.

6 Summary

In this study we developed a framework for the assessment of sudden changes in sea ice drift in response to atmospheric forcing and ice-coast interactions based on beacons deployed in a triangular configuration as triplets and Lagrangian dispersion analyses. The diagnostics and tools developed provided a unique characterization of sea ice drift and deformation processes in the southern Beaufort Sea, with implications for ice hazard assessments and forecasting applications.

Formatted: Font:Not Italic

Deleted: .

Formatted: Indent: First line: 1.27 cm

Deleted: 5 Discussion ... [5]

Deleted: Conclusions

Deleted: three-particle

Deleted: quantifying "shock-response" systems relevant for

Sudden changes in sea ice drift on daily timescales provide a signature of sea ice response to atmospheric forcing. In response to our first research question, single-particle dispersion statistics were used to identify sudden changes in ice drift paths, captured also in the three-day running means in variances of triplet centroid positions. Absolute dispersion also highlights the existence of two ice dynamical regimes prior to and following the 8 October SLP high responsible for Ekman convergence, poleward retreat in the ice edge, and resulting in the subsequent loss in both ice-atmosphere synchronicity and spatial coherence in triplet events. Demonstrated also are changes in ice concentrations during sudden changes, with lower ice concentrations for all triplets during the early stages of evolution, and for triplet B following the 8 October SLP high. Sudden changes reflect sea ice drift responses to SLP low and high regimes; regional differences are manifested predominantly in turning angles, the local characterizations of which are explored in an assessment of triplet area, deformation (DKPs), and relative deformation.

In response to our second research question, sea ice deformation is characterized in this study by two- and three-particle dispersion, including evolution in triplet area, perimeter-to-area ratio, the Okubo-Weiss criterion to monitor relative contributions from vorticity (due to external forcing) and deformation (associated with distortion in the ice cover), in addition to the shear-to-divergence ratio as a signature of sea ice stress and strength in the ice cover. Triplet areas depict local responses due to ice strength and drift. Triplet area during sudden changes demonstrates an increase in triplet A near the ice edge, and enhanced stretching closest to the shoreline. DKPs further show that sea ice deformation is weakest furthest from the coastline. Relative DKPs highlight enhanced distortion in the (bounded) ice cover encountered by Triplet B, located closest to the coastline, particularly following the SLP high on 8 October that led to a fragmented ice cover and reduced ice concentrations.

Results from this analysis suggest that sudden changes in the southern Beaufort Sea occur either during i) a reversal in winds that induce onshore/offshore ice drift, or ii) sustained north/easterly winds, with response mechanisms governed by ice conditions and interactions with the coastline. Sudden changes associated with wind reversals (minima in drift variance and inflection points in absolute dispersion; *e1*, *e3*, *e4*, *e6*, and *e8*) occur during SLP gradients. Changes in ice stress monitored by shear-

Deleted: s

Deleted: we identified eight sudden changes

Deleted: by temporal discontinuities

Deleted: 'Shock' parameters used to evaluate sudden changes in ice drift included SLP and turning angles, SAT and SIC in the vicinity of triplet centroids, in addition to NARR winds, ice drift and orientation. Comparison of drift variance and SLP mean time series in the vicinity of the triplets indicate that the "shock-response" mechanism occurs with SLP gradients, while turning angles and shock events provide an initial and regional indication of sea ice mechanics and deformation due to interactions with the coastline. Winds and ice drift illustrate a shear shock event (SSE) on 8 October due to easterly winds within a high ice concentration regime, resulting in strong offshore ice drift, and

Deleted: SSE

Deleted: ... [6]

Deleted: s

Deleted: investigation of sea ice deformation events during sudden changes illustrated local changes in sea ice cover based on interactions with the coastline, and distance relative to the coastline.

Deleted: 'Response' parameters and diagnostics included the evolution

Deleted:

Deleted: shear shock event

Deleted: Regional differences in triplet events are captured by turning angles, and local differences by DKPs, the OW criterion, and shear-to-divergence ratio.

Deleted: strength

Deleted: evident in

to-divergence ratios are associated with the transition from an on or offshore to along-shore ice drift regime. Triplet D, located furthest from the coastline, is uninfluenced by ice-coast interactions.

In summary, single-particle dispersion captures i) a shift in ice dynamical regimes following the 8 October SLP high, ii) inflection points and sudden changes in the meridional direction associated with interactions with the coastline, and iii) loss of coherence in ice-atmosphere interactions to provide a regional characterization of sea ice drift. Two- and three-particle dispersion capture i) sea ice deformation induced by northeasterly winds and accompanying along- and cross-shear transport ii) relative DKPs and enhanced deformation with decreasing distance from the coastline following the 8 October event, and iii) local and regional variations in sea ice deformation in the ice cover relevant for rheological characterizations of sea ice based on an assessment of the shear-to-divergence ratios.

Results from this analysis provide a prescription for identifying sudden changes in the ice drift field and accompanying changes in deformation characteristics based on distance from the coastline and proximity to the ice edge (where ice drifts more freely) relevant for prediction and ice-hazard detection on daily timescales. Proposed future work includes the use of the shock-response parameters, and Okubo-Weiss criterion and shear-to-divergence ratio diagnostics in particular for model-data comparison in applications involving ice hazard detection, forecasting and prediction. Numerical experiments testing sea ice response to sudden changes in ice drift during SLP high and low regimes will provide additional insight into physical mechanisms responsible for the observed local kinematic and deformation features in the ice drift field.

Lagrangian dispersion thus provides a framework and prescription for understanding sea ice dynamics that will enable the construction of an integrated observational-modeling framework designed specifically to understand ice-atmosphere interactions in the context of drift and deformation. Furthermore, an understanding of floe size shapes and distributions prior to, during, and following sudden changes in the ice drift cover using these diagnostics, and shear-to-divergence ratio in particular, will improve our understanding of how the sea ice cover responds to atmospheric forcing based on distance from the coastline. Results from this analysis can be applied to develop an observational-modeling framework for Lagrangian dispersion that monitors sea ice drift and deformation at large,

Deleted: Noteworthy also is the existence of a sudden change due to easterly winds within a consolidated ice regime which induced strong offshore ice drift on 8 October and precipitated a decline in the ice cover near the ice edge encountered by triplet B.

Deleted: Sudden changes associated with maxima or inflection points in ice drift variance (*e2*, *e5*, and *e7*) occur during persistent northerly/northeasterly winds. Results suggest that vorticity superimposed on shear weakens ice strength, and that following vorticity, a 'folding' occurs that appears associated with a strengthening in the ice cover, in a manner similar to mechanical annealing. Alternating cyclonic/anticyclonic regimes in triplets A and B and to a lesser extent C further suggest a folding mechanism within the bounded ice regime located closest to the coastline. These results raise the question as to whether vorticity anticipates a stronger ice cover.

Formatted: Highlight

Deleted: shock events

Deleted:

Deleted: The identification of two distinct categories of sudden changes or shock events (reversals and northerly/northeasterly), and conditions necessary for a strong offshore ice drift event will enable the construction

Deleted: Also of interest is improved understanding of the simulated annealing mechanism associated with persistent northerly winds and along-shore ice drift.

Deleted: and interaction with

regional, and local spatial scales. Implications for EVP and rheological characterizations of sea ice using observations, results and diagnostics from this investigation could further be explored.

Proposed work using results from this study includes efforts to address the question: What are the implications of changing ice and atmospheric patterns and dynamics for ice –atmosphere interactions, including heat and momentum exchange in particular, and local and global-scale processes more generally?

Acknowledgements

Buoy data were funded by the Natural Sciences and Engineering Research Council of Canada, the Canada Foundation for Innovation and partner organizations. Funding for this study was also provided by the Canadian Networks of Centres of Excellence (NCE) program, and Canada Research Chairs (CRC) programme (D.G. Barber). The authors would like to thank D. Babb and R. Galley for triplet deployment and for contributions to an earlier version of this manuscript. This work was completed as a contribution to the ArcticNet and Arctic Science Partnership networks.

References

Bouillon, S. and Rampal, P.: On producing sea ice deformation data sets from SAR-derived sea ice motion, The Cryosphere, 9, 663-673, doi:10.5194/tc-9-663-2015, 2015.

Barber, D. G., Galley, R., Asplin, M.G., De Abreu, R., Warner K.-A., Pućko, M., Gupta, M., Prinsenberg S., Julien, S.: Perennial pack ice in the southern Beaufort Sea was not as it appeared in the summer of 2009, Geophys. Res. Lett., 36, L24501, doi:10.1029/2009GL041434, 2009.

Bourassa, M. A., Gille, S. T., Bitz, C., Carlson, D., Clayson, C. A., Cerovecki, I., Cronin, M. F., Drennan, W. M., Fairall, C. W., Hoffman, R. N., Magnusdottir, G., Pinker, R. T., Renfrew, I. A., Serreze, M., Speer, K., Talley, L. D., and Wick, G. A.: High-latitude ocean and sea ice surface fluxes: Challenges for climate research. Bulletin of the American Meteorological Society, 94, 3, 403-423, 2013.

Carleton, A. M.: Synoptic sea ice-atmosphere interactions in the Chukchi and Beaufort Seas from NIMBUS 5 ESMR data, J. Geophys. Res., 89, D5, 7245–7258, doi:10.1029/JD089iD05p07245, 1984.

Formatted: Font:Times New Roman, 12

Formatted: Font:Times New Roman, 12

Formatted: Left, No widow/orphan control, Don't adjust space between Latin and Asian text, Don't adjust space between Asian text and numbers

Formatted: No widow/orphan control, Don't adjust space between Latin and Asian text, Don't adjust space between Asian text and numbers

Formatted: Font:(Default) +Theme Body, 12 pt

Formatted: Font:(Default) +Theme Body, 12 pt

Formatted: Font:(Default) +Theme Body, 12 pt

Formatted: Font:(Default) +Theme Body, 12 pt

Formatted: Font:(Default) +Theme Body, 12 pt

Formatted: Font:(Default) +Theme Body, 12 pt

Formatted: Font:(Default) +Theme Body, 12 pt

Formatted: Font:(Default) +Theme Body, 12 pt

Formatted: Font:(Default) +Theme Body, 12 pt

Formatted: Font:(Default) +Theme Body, 12 pt

Formatted: Font:(Default) +Theme Body, 12 pt

Formatted: Font:(Default) +Theme Body, 12 pt

Carmack, E., Polyakov, I., Padman, L., Fer, I., Hunke, E., Hutchings, J., Jackson, J., Kelley, D., Kwok, R., Layton, C., Melling, H., Perovich, D., Persson, O., Ruddick, B., Timmermans, M.-L., Toole, J., Ross, T., Vavrus, S., and Winsor, P.: Toward quantifying the increasing role of oceanic heat in sea ice loss in the new Arctic, Bulletin of the American Meteorological Society, 96,12, 2079-2105, 2015.

Colony, R. and Thorndike, A.S.: An estimate of the mean field of Arctic sea ice motion, J. Geophys. Res., 89, C6, 10,623–10,629, doi:10.1029/JC089iC06p10623, 1984.

Colony, R. and Thorndike, A.S.: Sea ice motion as a drunkard's walk, J. Geophys. Res., 90, C1, 965–974, doi:10.1029/JC090iC01p00965, 1985.

Geiger, C.A., Ackley, S.F., and Hibler III, W.D.: Sea ice drift and deformation processes in the western Weddell Sea, in *Antarctic Sea Ice: Physical Processes, Interactions and Variability*, Antarct. Res. Set., vol. 7, pp. 141-160, edited by M.O. Jeffries, AGU, Washington, D.C., 1998.

Geiger, C.A., Zhao, Y., Liu, A.K., and Hakkinen, S.: Large-scale comparison between buoy and SSM/I drift and deformation in the Eurasian Basin during winter, 1992 – 1993, J. Geophys. Res., 105, C2, 2257 – 3368, 2000.

Geiger, C.A. and Drinkwater, M.R.: Impact of temporal-spatio resolution on sea-ice drift and deformation, IUTAM Symposium on Scaling Laws in Ice Mechanics and Dynamics, (eds.) J.P. Dempsey and H.H. Shen, Kluwer Academic Publishers, Netherlands, 407-416, 2001.

Geiger, C. A. and Perovich, D.K.: Springtime ice motion in the western Antarctic Peninsula region, Deep-Sea Res. II, 55, 338 – 50, 2008.

Gherardi, M. and Lagomarsino, M.C.: Characterizing the size and shape of sea ice floes, Nature, Scientific Reports 5, 10226, doi: 10.1038/srep10226, 2015.

Guest P. S. and Davidson, K.L.: The aerodynamic roughness of different types of sea ice. J. Geophys. Res. 96, C3, 4709–4721, 1991.

Hakkinen, S.: Coupled ice–ocean dynamics in the marginal ice zones: upwelling/downwelling and eddy generation. J.Geophys. Res. 91, C1, 819–832, 1986.

Hakkinen, S., Proshutinsky, A., Ashik, I.: Sea ice drift in the Arctic since the 1950s, Geophys. Res. Lett., 35, L19704, doi:10.1029/2008GL034791, 2008.

Heil, P. and Hibler, W.D.: Modeling the high-frequency component of Arctic sea ice drift and deformation, J. Phys. Oceanography, 32, 3039 – 3057, 2002.

Formatted: Font:12 pt

Formatted: Font:12 pt

Formatted: Font:12 pt

Formatted: Font:12 pt

Formatted: Left, No widow/orphan control, Don't adjust space between Latin and Asian text, Don't adjust space between Asian text and numbers

Formatted: Font:12 pt

Formatted: Font:English (US)

Heil, P., Hutchings, J.K., Worby, A.P., Johansson, M., Launiainen, J., Haas, C., and Hibler, W.D.: Tidal forcing on sea-ice drift and deformation in the western Weddell Sea in early austral summer, 2004, Deep-Sea Res., Part II – Topical studies in oceanography, 55, 8-9, 943-962, 2008.

Heil, P., Massom, R.A., Allison, I., Worby, A.P., and Lytle, V.I.: Role of off-shelf to on-shelf transitions for East Antarctic sea ice dynamics during spring 2003, J. Geophys. Res. – Oceans, 114, C09010, doi:10.1029/2008JC004873, 2009.

Heil, P., Massom, R.A., Allison, I., Worby, A.P.: Physical attributes of sea-ice kinematics during spring 2007 off East Antarctica, Deep-Sea Res., Part II- Topical studies in oceanography, 58, 9-10, 1158 – 1171, 2011.

Hutchings, J. K., Heil, P., Hibler III, W. D.: On modelling linear kinematic features in sea ice. Monthly Weather Review, 12, 3481-3497, 2005.

Hutchings, J.K., Roberts, A., Geiger, C., and Richter-Menge, J.: Spatial and temporal characterization of sea-ice deformation, Ann. Glaciol., 52,57 Pt 2, 360–368, doi: 10.3189/2011AoG57A185, 2011.

Hwang, P. A.: Temporal and spatial variation of the drag coefficient of a developing sea under steady wind-forcing. J. Geophys. Res., 110, C07024, doi:10.1029/2005JC002912, 2005.

Kwok, R., Contrasts in sea ice deformation and production in the Arctic seasonal and perennial ice zones, J. Geophys. Res., 111, C11S22, doi:10.1029/2005JC003246, 2006.

Kwok, R. and Cunningham, G. F.: Deformation of the Arctic Ocean ice cover after the 2007 record minimum in summer ice extent, CRST, 76-77, doi: 10.1016/j.coldregions.2011.04.003, 2012.

LaCasce, J.H.: Lagrangian statistics from oceanic and atmospheric observations, Lect. Notes Phys., 744, 165-218, 2008.

Lawrence Berkeley National Laboratory (2008, January 3), Mechanical Annealing, Increased Strength and Why Materials Get Stronger as They Get Smaller. Retrieved from http://www.azonano.com/article.aspx?ArticleID=2045.

LeDrew, E.F., Johnson, D., Maslanik, J.A.: An examination of atmospheric mechanisms that may be responsible for the annual reversal of the Beaufort Sea ice field. Int. J. Clim. 11, 841–859, 1991.

Lukovich, J., Geiger, C.A., Babb, D., Galley, R., and Barber, D.G.: Ice beacon triplet deployments in the Beaufort Sea gyre, 2009 Arctic Net Ice Beacon GPS Positions and Centroid Triplet Arrays, Centre for Earth Observation Science, Canadian Cryospheric Information Network Reference Number 12709, Polar Data Catalogue, 2016.

Formatted: Font:12 pt

Formatted: Font:12 pt

Formatted: Font:12 pt

Formatted: Font:12 pt

Deleted: -

Formatted: Font:12 pt, Font color: Custom Color(RGB(33,151,210))

Lukovich, J.V., Babb, D.G., and Barber, D.G.: Ice beacon trajectories in the Arctic during the IPY-CFL study, J. Geophys. Res., doi:10.1029/2011JC007049, 2011.

Lukovich, J.V., Belanger, C., Barber, D.G., and Gratton, Y.: On coherent ice drift features in the Beaufort Sea gyre, *Deep Sea Res*., Part I: Oceanographic Research Papers, 92, 56 – 74, 2014.

Lukovich, J.V., Hutchings, J.K., and Barber, D.G.: On sea ice dynamical regimes in the Arctic Ocean, *Annals of Glaciology*, 56, 69, 323 – 331, 2015.

McPhee, M.G.: Advances in understanding ice–ocean stress during and since AIDJEX, Cold Regions Science and Technology, Volumes 76–77, 24-36, http://dx.doi.org/10.1016/j.coldregions.2011.05.001, 2012.

Mesinger, F., DiMego, G., Kalnay, E., Mitchell, K., Shafran, P.C., Ebisuzaki, W., Jovic, D., Woollen, J., Rogers, E., Berbery, E.H., Ek, M.B., Fan, Y., Grumbine, R., Higgins, W., Li, H., Lin, Y., Manikin, G., Parrish, D., and Shi, W.: North American regional reanalysis, Bulletin of the American Meteorological Society, 87, 3, 343 – 360, 2006.

Molinari, R. and Kirwan, A.D.: Calculations of differential kinematic properties from Lagrangian observations in western Caribbean Sea, J. Physical Oceanography, 5, 3, 483-491, 1975.

Okubo, A.: Horizontal dispersion of floatable particles in the vicinity of velocity singularities such as convergences, Deep Sea Res., 17, 445–454, 1970.

Overland, J., Walter, B., Curtin, T. B., and Turet, P.: Hierarchy and sea ice mechanics: A case study from the Beaufort Sea, J. Geophys. Res., 100, C3, 4559 – 4571, 1995

Polar Group, The: Polar atmosphere-ice-ocean processes: A review of polar problems in climate research, Rev. Geophys.,18, 2, 525–543, doi:10.1029/RG018i002p00525, 1980.

Preller, R. B., and Posey, P.G.: A numerical model simulation of a summer reversal of the Beaufort Gyre, Geophys. Res. Lett., 16, 69– 72, 1989.

Prinsenberg, S.J., Fowler, G.A., van der Baaren, A.: Pack ice convergence measurements by GPS-ARGOS ice beacons, Cold Regions Science and Technology, 28, 2, 59-72, doi: 10.1016/S0165-232X(98)00013-5, 1998.

Proshutinsky, A., Dukhovskov, D., Timmermans, M.-L., Krishfield, R., Bamber, J.L.: Arctic circulation regimes, Phil. Trans. R. Soc. A, 373, 1 – 18, doi:10.1098/rsta.2014.0160, 2015.

Formatted: Font:12 pt
Formatted: Font:12 pt
Formatted: Font:12 pt
Deleted:
Formatted: Font:12 pt
Deleted:

Rampal, P., Weiss, J., Marsan, D., Lindsay, R., and Stern, H.: Scaling properties of sea ice deformation from buoy dispersion analysis, J. Geophys. Res., 113, C03002, doi:10.1029/2007JC004143, 2008.

Rampal, P., Weiss, J., Marsan, D., and Bourgoin, M.: Arctic sea ice velocity field: General circulation and turbulent-like fluctuations, J. Geophys. Res., 114, C10014, doi:10.1029/2008JC005227, 2009a.

Rampal, P., Weiss, J., and Marsan, D.: Positive trend in the mean speed and deformation rate of Arctic sea ice, 1979–2007, J. Geophys. Res., 114, C05013, doi:10.1029/2008JC005066, 2009b.

Richter-Menge, J. A., McNutt, S. L., Overland, J. E., and Kwok, R.: Relating Arctic pack ice stress and deformation under winter conditions, J. Geophys. Res., 107, C10, 8040, doi:10.1029/2000JC000477, 2002.

Saucier, W.J.: Principles of meteorological analysis, University of Chicago Press, Chicago, IL, 438 pp., 1955.

Shan, Z.W., Mishra, R.K., Sayed Asif, S.A., Warren, O.L., Minor, A.M.: Mechanical annealing and source-limited deformation in submicrometre-diameter Ni crystals, Nature Materials 7, 115 – 119, 2007.

Spreen, G., Kwok, R., Menemenlis, D.: Trends in Arctic sea ice drift and role of wind forcing: 1992–2009. Geophys. Res. Lett. 38, L19501, http://dx.doi.org/10.1029/2011GL048970, 2011.

Stern H.L. and Lindsay, R.W.: Spatial scaling of Arctic sea ice deformation. J. Geophys. Res., 114, C10, C10017, doi:10.1029/2009JC005380a, 2009.

Stroeve J., Serreze M, Drobot S, Gearheard S, Holland M, Maslanik J, Meier W, and Scambos T.: Arctic sea ice extent plummets in 2007. EOS, Trans. Am. Geophys. Union 89, 13–14, doi:10.1029/2008EO020001), 2008.

Taylor, G. I.: Diffusion by continuous movements, Proc. London Math. Soc., s2-20, 196–212, doi:10.1112/plms/s2-20.1.196, 1921.

Thorndike, A. S.: Kinematics of sea ice, The Geophysics of Sea Ice, NATO ASI Ser., Ser. B, 146N. Untersteiner, Plenum, New York., 489–549, 1986.

Wadhams et al.: Basin-scale ice motion and deformation in the Weddell Sea in winter, Annals of Glaciology, 12, 178 – 186, 1989.

Weiss, J.: The dynamics of enstrophy transfer in two-dimensional hydrodynamics, Physica D, 48, 273–294, 1991.

Formatted: Font:12 pt

Formatted: Font:12 pt

Formatted: Left, No widow/orphan control, Don't adjust space between Latin and Asian text, Don't adjust space between Asian text and numbers

Formatted: Font:12 pt

Field Code Changed

Formatted: Hyperlink, Font:12 pt, Font color: Auto, English (UK)

Formatted: Font:Font color: Black, English (US)

Weiss, J.: Drift, deformation, and fracture of sea ice, Springer Briefs in Earth Sciences, Springer Netherlands, Dordrecht Netherlands, doi:10.1007/978-94-007-6202-2 5, 2013.

Weiss J, Dansereau V.: Linking scales in sea ice mechanics. Phil. Trans. R. Soc. A 375: 20150352, 2017.

Formatted: Font:12 pt

Formatted: Font:12 pt

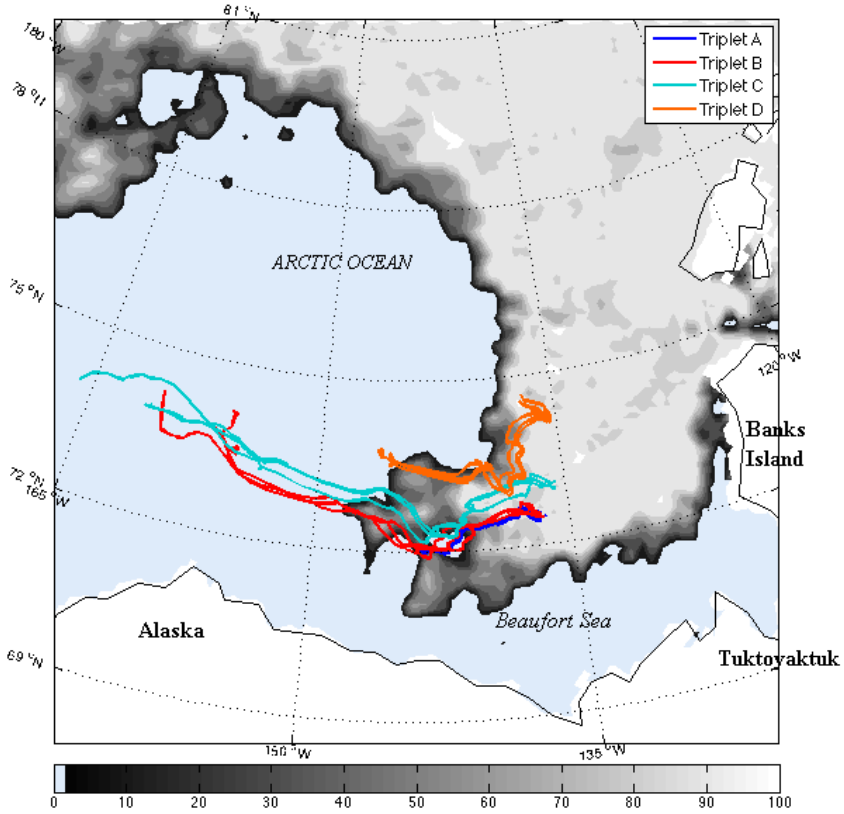

Figure 1a: GPS buoy-array-triplet trajectories relative to sea ice and coastline. Evolution in triplet A to D centroid trajectories, superimposed on sea ice concentration map in early September, 2009 on triplet deployment, with triplet A located closest to the coastline, and triplet D located furthest from the coastline. Triplet D is also initially located nearest the tongue of multiyear ice edge.

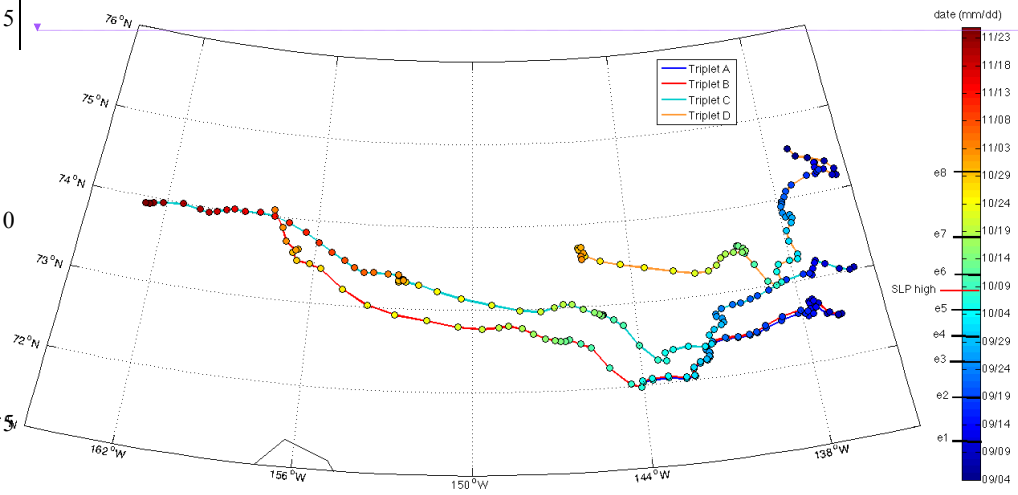

Figure 1b: Temporal evolution of triplet centroids A to D, colour-coded by date with each shock event enumerated in the colourbar timeline. The SLP high resulting in strong offshore ice drift, and decoupling in ice-atmosphere interactions is also depicted.

Deleted: <sp>

Deleted: Shear Shock Event (SSE) associated with easterly winds during a

Deleted: and high ice concentration regime,

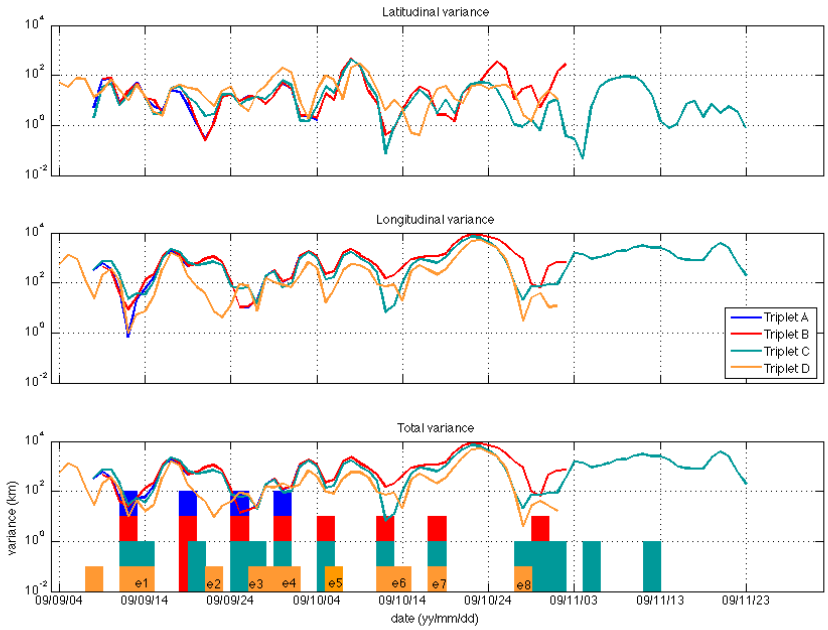

Figure 2: Abrupt changes in triplet A to D centroid trajectories, defined as minima in the variances of the 3-day running mean triplet centroid positions. The upper, middle, and lower panels depict latitudinal, longitudinal and total variance, respectively. SSE depicts the shear shock event associated with strong offshore ice drift. Comparison with mean SLP in the vicinity of the triplets shows correspondence between SLP and drift variance maxima prior to SSE; minima occur between SLP and variance maxima.

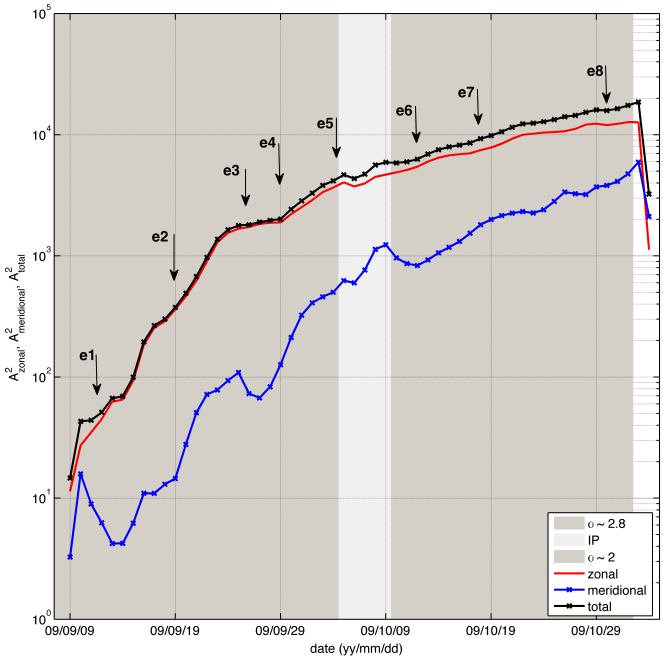

Figure 3: Absolute (single-particle) dispersion statistics for triplets A to D, depicting zonal (red), meridional (blue), and total (black) dispersion. Light shaded area depicts inflection point (IP) range, and dark shaded areas dynamical regimes associated with $\alpha \sim 3$ and $\alpha \sim 2$ prior to and following the inflection point range, capturing increased contributions from meridional drift. Arrows and labels depict triplet events derived from the variance analysis.

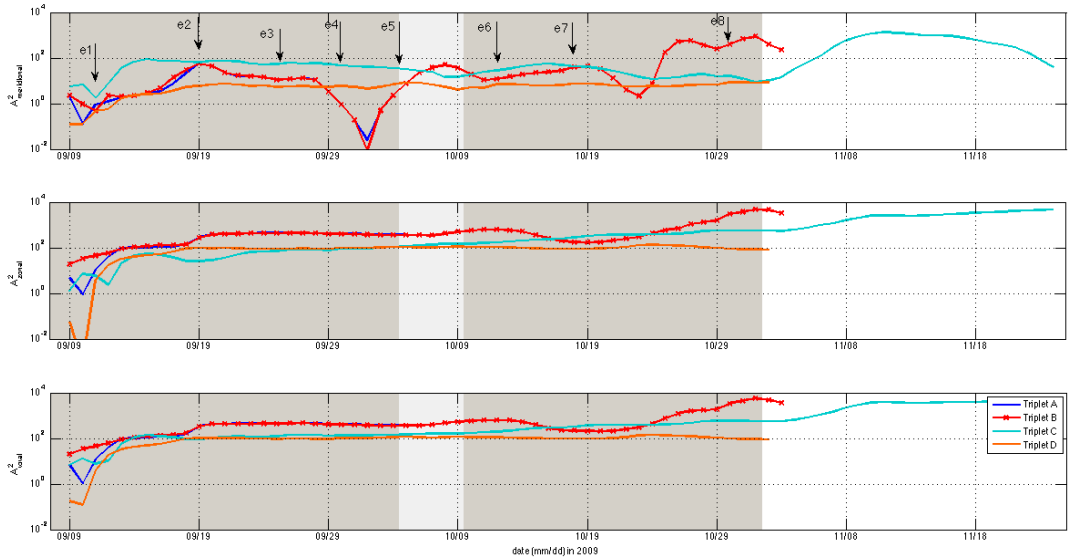

Figure 4a: Absolute (single-particle) dispersion statistics depicting meridional (top), zonal (middle), and total (lower) dispersion for individual triplets A (blue), B (blue), C (cyan) and D (amber) based on inter-beacon distances, to characterize local changes in ice drift. Shading and arrows are as in Figure 3 providing a regional characterization.

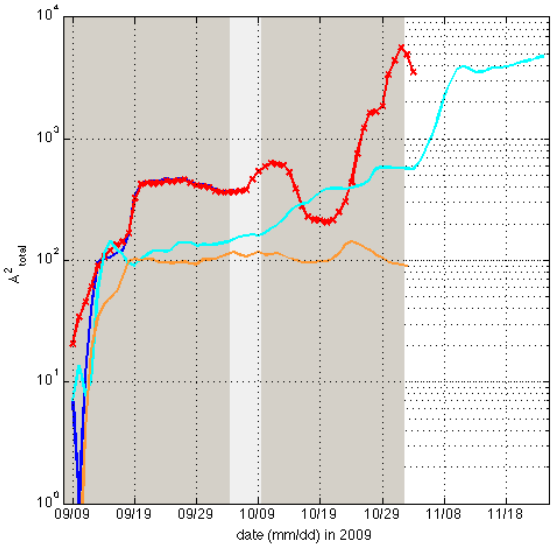

Figure 4b: Total single-particle dispersion for triplets A (blue), B (red), C (cyan), and D (amber) as an enlargement of lower panel in Figure 4a, capturing temporal evolution in and differences between triplet slopes based on local beacon behaviour associated with each triplet.

Deleted: <sp>

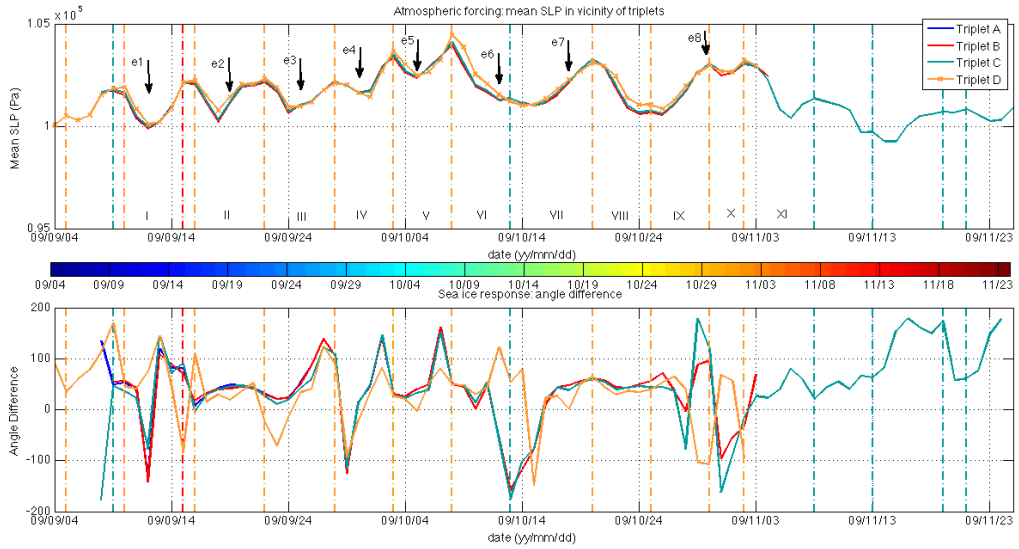

Figure 5: Atmospheric forcing and regional sea ice response. Mean SLP in the vicinity of triplets A to D highlighting atmospheric forcing (upper panel). Turning angle between surface winds and triplet centroid drift depicting sea ice response (lower panel). Colour bar indicates colours associated with centroid dates in Figure 1b.

Deleted: .

Deleted: <sp>

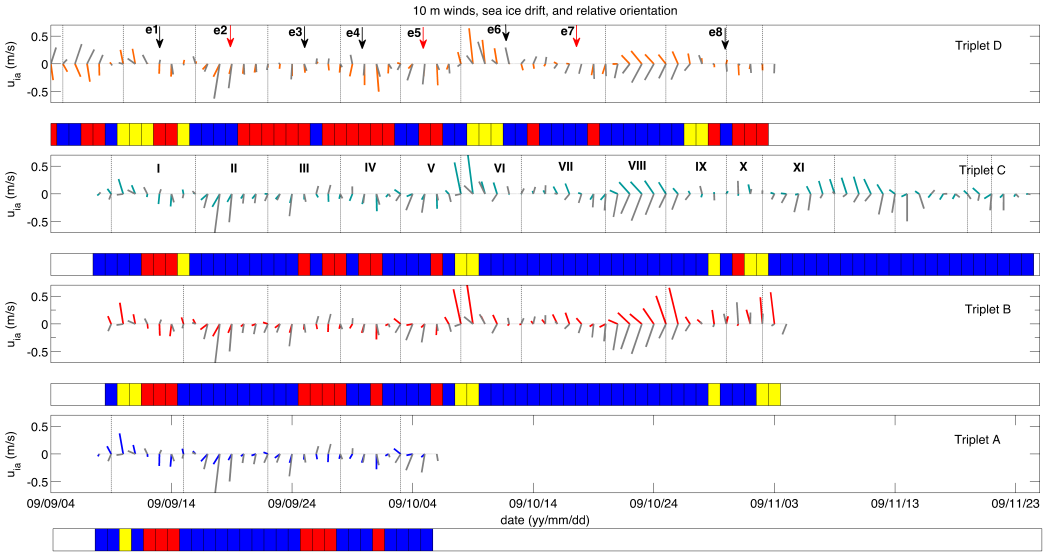

Figure 6: Winds, sea ice drift and orientation relative to the coastline. Time series of 10 m North American Regional Reanalysis (NARR) winds in the vicinity of the triplet centroids (grey vectors), sea ice drift for triplets A (lowermost panel) to D (uppermost panel), and offshore (yellow), onshore (red), and alongshore (blue) ice drift orientation.

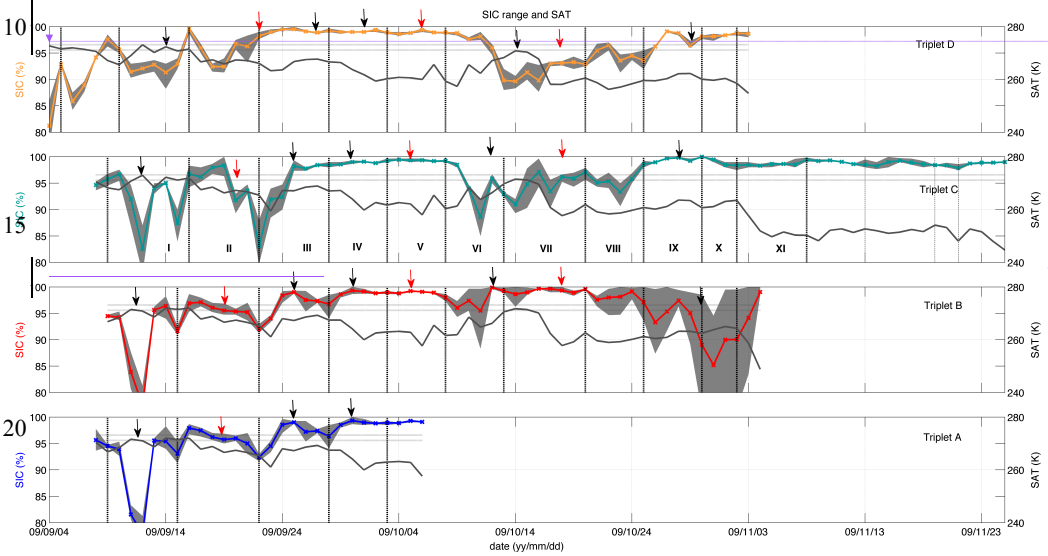

Figure 7: Sea ice concentration (SIC) range and Surface Air Temperatures (SAT). Time series of percent sea ice concentration and SAT for triplets A (lowermost panel) to D (uppermost panel). Vertical lines depict dates associated with SLP highs and roman numerals the SLP interval described in Table 3. Grey shading shows the range of ice concentrations encountered by three beacons comprising the triplets. Horizontal lines depict SAT values of 273 K and 275 K.

Deleted: ... [7]

Deleted: <sp>

Formatted: Tabs: 4.87 cm, Left

Formatted: Normal

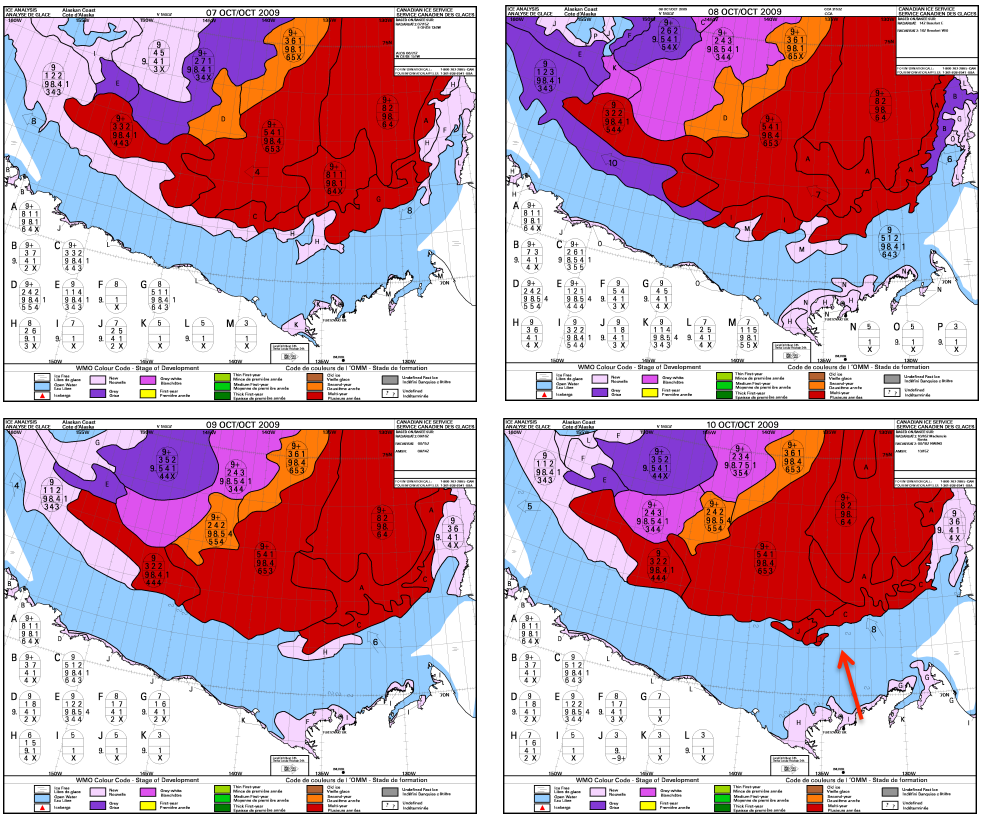

Figure 8: Canadian Ice Service ice charts showing sea ice development stages on 7, 8, 9, and 10 October prior to, during, and following the 8 October SLP high. Noteworthy is the poleward retreat in the ice edge on 10 October due to sea ice convergence associated with the SLP high.

Formatted: Normal

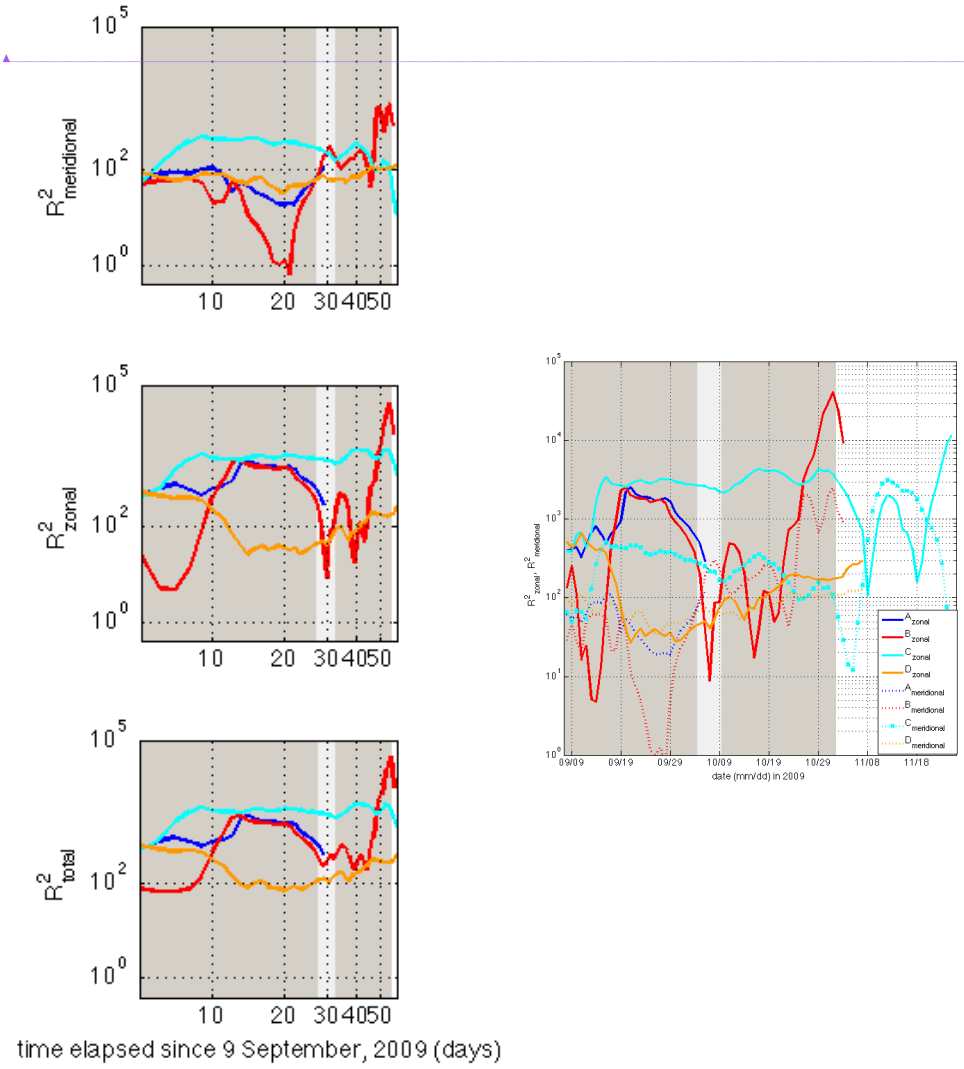

Figure 9 Relative (two-particle) dispersion showing (left column) meridional (top), zonal (middle), and total (lower panel) relative dispersion as a function of elapsed time since 9 September, 2009, and (right panel) a superposition of zonal (solid line) and meridional (symbol dashed line) relative dispersion.

Formatted: Normal

Formatted: English (UK)

Formatted: Caption

Formatted: English (UK)

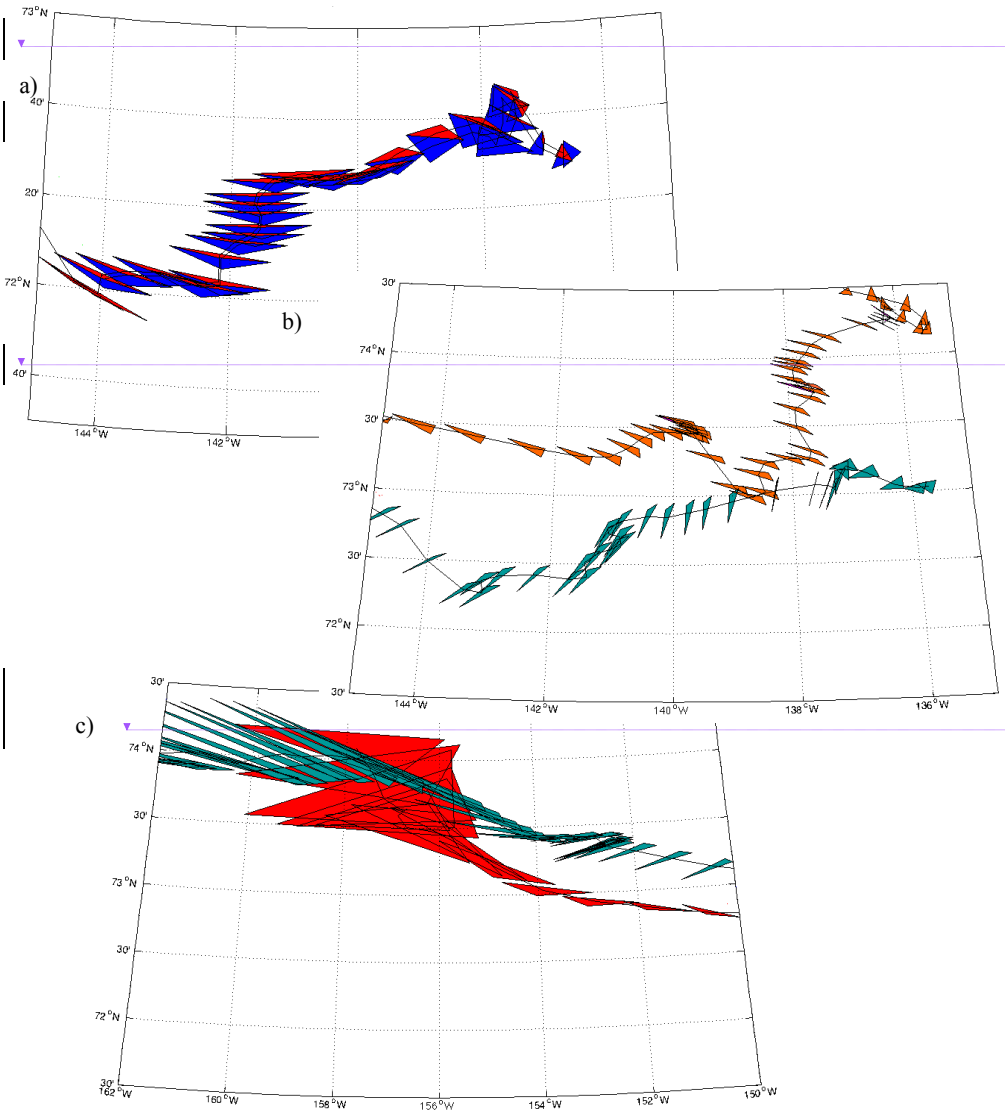

Figure 10: Triplet area evolution. Examples of triplet evolution for triplet A (blue triangle), B (red triangle), C (cyan triangle), and D (amber triangle), including (a) initial evolution in triplets A and B, (b) evolution in triplets C and D, (c) final evolution in triplets B and C.

Deleted: <sp>

Deleted: <sp>

Deleted: <sp>

Deleted:

Formatted: Caption

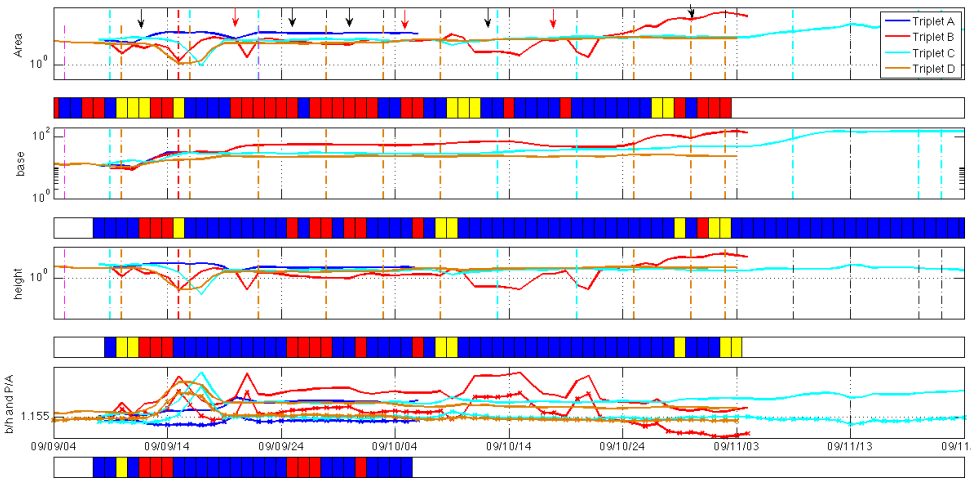

Figure 11: Triplet area evolution. Time series of triplet area, base, height, base-to-height and perimeter-to-area ratios for triplets A to D. Solid lines in lower panel depict the base-to-height ratio, while the lines with symbols depict the perimeter-to-area ratio. The value for the base-to-height ratio associated with an equilateral configuration (1.155) is also shown. Horizontal bar graphs depict on-, along-, and offshore ice drift as depicted in Figure 7.

Deleted: b

Deleted: 5

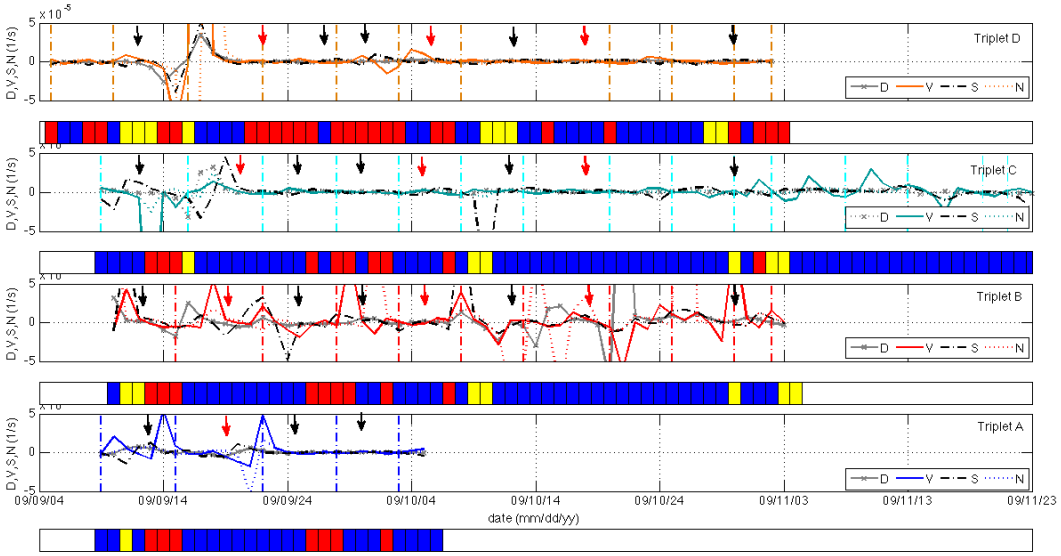

Figure 12: Sea ice deformation. Time series of Differential Kinematic Parameters (DKPs) divergence (D), vorticity (V), the shearing deformation rate (S), and the normal (stretching) deformation rate (N) for triplets A (lowermost panel) to D (uppermost panel). Vertical lines depict SLP high in the vicinity of each triplet centroid as shown in Figure 3. Horizontal bar graphs depict on-, along, and offshore ice drift as depicted in Figure 5.

Deleted: <*sp*>

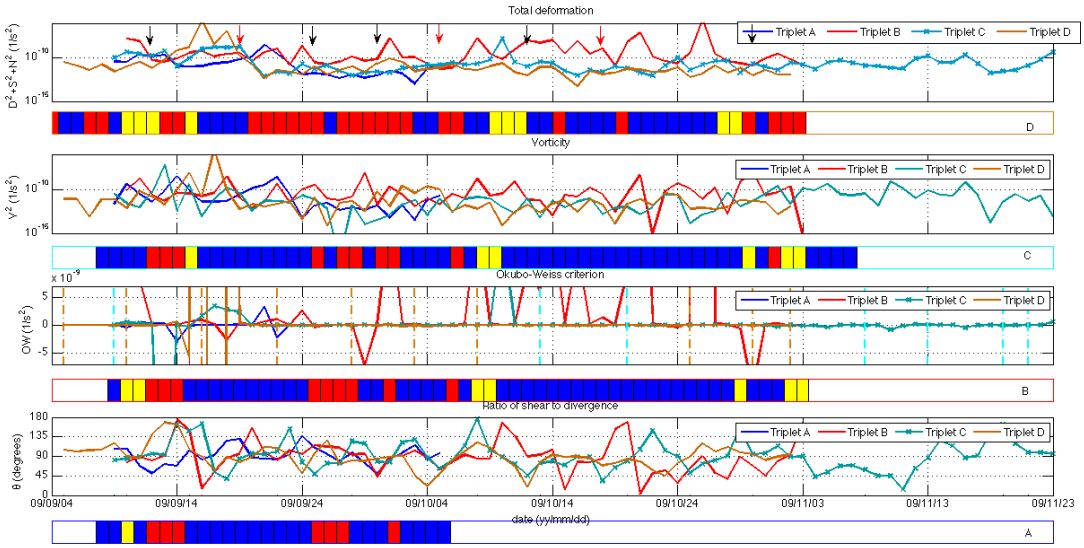

Figure 14: Relative sea ice deformation. Time series of relative sea ice deformation for Triplets A to D, including the total deformation ($D^2 + S^2 + N^2$), vorticity (V^2), Okubo-Weiss criterion capturing relative contributions of deformation and vorticity with OW > 0 indicating deformation-dominated flow and OW <0 indicating flow dominated by vorticity, and θ, or the arctan of the shear-to-divergence ratio to further distinguish deformation between shear and divergence-dominated regimes relevant for rheological characterizations.

Deleted: <sp>

Formatted: Tabs: 7.95 cm, Left

Deleted: 8

Deleted: Figure 8:

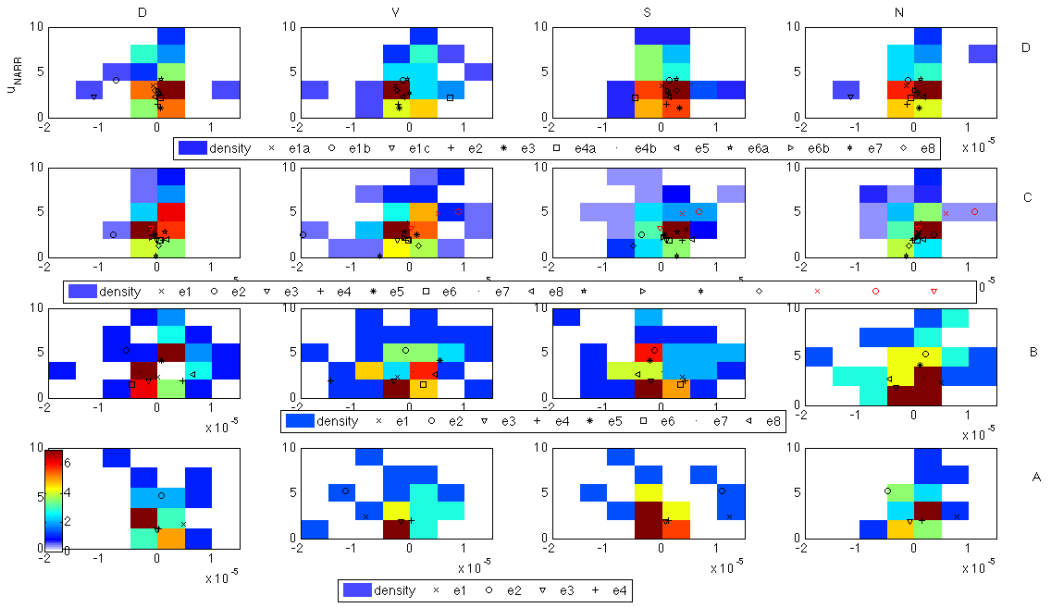

Figure 15: Scatter plots of NARR winds versus DKPs for triplets A to D showing number of triplet centroid values in the vicinity of and associated with NARR and DKP bins. Symbols depict sudden change events.

Table 1: Evolution in triplet A to D trajectories; triplet event dates and coordinates

Event/Triplet	Date (mm/dd)		Latitude		Longitude	
e1 – Initial "shock" and cusp in trajectory						
A	09/11	09/13	72.68	72.71	-137.47	-137.64
B	09/11	09/13	72.76	72.65	-137.34	-137.47
C	09/11	09/13	73.14	73.18	-136.74	-137.14
D	09/13	09/15	73.18	73.04	-137.14	-137.32
	09/11	09/13	74.26	74.36	-135.89	-136.18
	09/13	09/15	74.36	74.22	-136.18	-136.25
e2 – Second shock and southwestward migration						
A	09/18	09/20	72.57	72.46	-138.78	-139.72
B	09/18	09/20	72.65	72.62	-138.73	-139.74
C	09/19	09/21	72.96	72.88	-139.02	-139.75
D	09/21	09/23	74.02	73.95	-137.68	-137.84
e3 – Third shock and southward migration						
A	09/24	09/26	72.43	72.33	-141.34	-141.61
B	09/24	09/26	72.48	72.45	-141.37	-141.64
C	09/24	09/26	72.82	72.72	-140.87	-141.07
D	09/26	09/28	72.72	72.65	-141.07	-140.86
	09/26	09/28	73.78	73.75	-137.80	-137.55

5

Event/Triplet	Date		Latitude		Longitude	
e4 – Fourth shock and south- and westward migration						
A	09/29	10/01	72.22	72.14	-141.64	-142.15
B	09/29	10/01	72.39	72.32	-141.67	-142.17
C	09/29	10/01	72.62	72.52	-140.96	-141.44
D	09/28	09/30	73.75	73.62	-137.55	-137.89
	09/30	10/02	73.62	73.32	-137.89	-137.65
e5 – Fifth shock and northwestward migration						
A	--	--	--	--	--	--
B	10/04	10/06	72.32	72.24	-143.09	-144.00
C	10/04	10/06	72.41	72.36	-142.24	-143.10
D	10/05	10/07	73.23	73.02	-138.46	-138.47
e6 – Sixth shock and northwestward migration ; triplet D loop						
A	--	--	--	--	--	--
B	10/11	10/13	72.21	72.06	-146.08	-146.63
C	10/11	10/13	72.82	72.88	-144.83	-145.22
D	10/11	10/13	73.43	73.54	-139.63	-139.83
	10/13	10/15	73.54	73.47	-139.83	-139.57

5

Event/Triplet	Date		Latitude		Longitude	
e7 – Seventh shock and northwestward migration						
A	--	--	--	--	--	--
B	10/17	10/19	72.07	71.98	-147.77	-148.65
C	10/17	10/19	72.97	73.04	-145.89	-146.62
D	10/17	10/19	73.46	73.42	-140.04	-140.55
e8 – Eighth shock and northwestward migration; triplet C and D loop						
A	--	--	--	--	--	--
B	10/29	10/31	72.61	72.60	-156.67	-156.68
C	10/27	10/29	73.33	73.33	-152.50	-152.76
D	10/29	10/31	73.33	73.36	-152.76	-152.58
	10/27	10/29	73.61	73.71	-145.68	-145.92

Deleted: ... [8]

Table 2: DKPs and impact on triangles

Triangle feature	DKPs			
	D	V	S	N
Area	D	x*	x	
Orientation	x	V		x
Shape	x	x	S	N

*x indicates that the DKPs do not change the triangle feature

Deleted: Page Break

Page Break

Abrupt change date ... [9]

Deleted:

Abrupt change date ... [10]

Appendix A: Methodology to Derive Daily Positions, Triplet Arrays, Centroids, and Ice Drift from Telemetry Data

Geographical positions are recorded from global positioning (GPS) beacons explained in the data section. The observed temporal resolution of the beacon position data is two hours (dt = 2 hours). Daily average positions are calculated for the analysis and time series. The position data is subsequently used to compute drift components based on triplet centroid daily displacements.

A.1. Sea ice drift and triplet centroids

A four-step process was used to convert telemetry geographical position records into daily beacon averages, centroid locations, and sea ice drift. First, daily average positions were calculated from the two-hourly data for each beacon. Second, triplets were organized based on proximity to the coastline, inter-beacon distances, and overlapping time intervals. Triplets A and B, with two shared beacons, were selected to highlight differences in ice drift and deformation on scales comparable to inter-beacon separations.

Third, centroids are calculated using the coordinates of the three beacons comprising each triplet. Fourth, ice drift is computed from centroid displacements. Specifically, the geographical latitude and longitude decimal degrees are converted to horizontal ortho-linear metric distances, using the north polar azimuthal equal-area map centred on the North Pole. Thus for the Earth's radius $R = 6371.228\ km$, pixel size $C = 25.0675\ km$, latitude ϕ, longitude λ, row and column origin $r0 = s0 = 181$ for a $361x361$ grid, and

$$r = 2R \sin\lambda \sin\left(\frac{\pi}{4} - \frac{\phi}{2}\right)$$
$$s = -2R \cos\lambda \sin\left(\frac{\pi}{4} - \frac{\phi}{2}\right),$$

the speeds associated with the metric distances, $u_r = 10^3 \Delta r/(\Delta t)$ and $u_s = 10^3 \Delta s/(\Delta t)$, for $\Delta t = 24 \times 3600$(s), are transformed to zonal and meridional components such that

$$u = u_r \cos\lambda + v_r \sin\lambda$$
$$v = -u_r \sin\lambda + v_r \cos\lambda.$$

Appendix B: Triplet Observation Report

A description of observations and results determined from shock-response diagnostics is provided in this appendix as supplementary material to the results section. Results are categorized according to i) shock diagnostics (SLP, turning angle, surface winds, ice drift, SIC and SAT as depicted in Figures 3 to 5) used in identifying trajectory changes in ice drift paths, and ii) response diagnostics (triplet Areas, DKPs, relative DKPs and shear-to-divergence ratios as depicted in Figures 6 to 8) used in identifying sea ice deformation responses during sudden changes in ice drift paths.

B.2.1 Identifying trajectory changes in sea ice drift and deformation

Figure 3. – Atmospheric forcing and sea ice response – spatial variability

In the context of ice shock events, large turning angles are observed for triplets A, B, and C during a SLP low for shock *e1*. Shock events evident during a transition in SLP phase are also observed in turning angles for all triplets (Figures 2b and 3). Specifically, angle differences on the order of 40 degrees are observed during decreasing SLP for shock *e2*. Turning angles increase during a transition to a SLP high for *e3*, whereas for shock *e4* negative turning angles exist for decreasing SLP. A SLP low is observed between successive SLP highs when triplet A stops recording during *e5*. The triplet D centroid loop event during *e6* is manifested in differences in turning angles during a SLP low, in a manner distinct from other triplet turning angles. Slight differences in turning angles are observed during increasing SLP for *e7*. As for *e6*, differences in turning angles highlight spatial (relative to distance from the coastline) differences in sea ice response to external forcing as a SLP high enters the region in the vicinity of the beacon triplets. SLP mean time series in the vicinity of the triplets indicate that the "shock-response" mechanism occurs with SLP gradients and a transition between local SLP

high and low regimes. As will later be explored, turning angles and shock events additionally provide an initial indication of sea ice mechanics and deformation.

Figure 4. – NARR winds, sea ice drift and orientation – spatial variability

A southerly to northerly transition in 10 m winds is accompanied by onshore ice drift for triplets A to C, and a second reversal from northerly to southerly winds accompanied by offshore ice drift for triplet D during *e1 (Figure 4)*. Strong northerly flow is observed in the vicinity of all triplets with alongshore (southwestward) drift in triplet A to C centroids, and onshore drift in triplet D during *e2*. Reversals in 10 m winds are observed with accompanying alongshore/onshore ice drift during *e3*. An interruption to the centroid trajectory is further observed during reversals in 10 m winds during *e4*, with along-shore and predominantly onshore drift for triplet D. By contrast, dominant northerly winds result in along-shore flow for all centroids during *e5*. Reversals in 10 m winds in the vicinity of triplets B and C with accompanying alongshore flow, and predominantly southerly winds in the vicinity of triplet D during a loop event highlight regional and local responses during *e6*. Northeasterly winds and alongshore ice drift for triplets B and C, and onshore drift for triplet D further highlights local responses during *e7*. Differences in winds and drift response are again observed during shock event *e8*.

Figure 5. – SIC range and SAT – spatial variability

In consideration of shock events, SIC values of ~80% with SAT less than zero degrees Celsius are observed for triplets A and B; SIC values of ~80% and ~90% with SAT less than two degrees Celsius are observed for triplets C and D respectively during *e1*. SIC ranges from 90 – 100 % and SAT is less than two degrees Celsius for all triplets during *e2*. Similarly during *e3*, SIC ranges from 95 – 100 % with SAT < 0 for all triplets. SIC approaches 100% concentration with SAT < 0 for shock events *e4* and *e5*. Lower ice concentrations for *e6* followed by an increase in SAT suggest an opening of leads in the vicinity of triplets B and C. A delayed response is observed for triplet D. During *e7* equilibration in SAT is accompanied by SIC values ranging from 90 – 100% for triplets B, C, and D. By contrast,

during *e8* SIC values are less than 80% as SAT increases for triplet B near the ice edge, while triplets C and D approach 100% ice concentration as SAT equilibrates and continues to decrease, respectively.

B.2.2 Identifying responses in sea ice deformation

Figure 6 Triplet area evolution

An assessment of evolution in triplet area during each of the sudden changes demonstrates an increase in triplet A area near the ice edge in contrast to decreasing areas for all other triplets during *e1*, with a lagged response in the maxima (Figure 6). The greatest stretching is also observed closest to the coastline. During *e2*, the base for triplets A and B increases during consolidation following which a maximum is achieved on the 21st (~ 2-day time lag). By contrast, P/A and b/h are approximately constant for triplets C and D, indicating that the triangle maintains its shape further from the continental coastline. Triplets A, C, and D maintain their shape during *e3*, while triplet B area decreases as the height decreases (P/A and b/h increase). During *e4*, P/A and b/h are constant for triplets A, C, and D with higher values further from the coastline (associated with smaller areas). A decline in P/A and b/h due to restoration in height is observed for triplet B. During *e5*, the area and ratios are approximately constant for all triplets, following which triplet A beacons stop recording. The greatest stretching (high base and ratio values) is observed in triplet B located closest to the shoreline/continental coastline. The area in triplet B decreases during *e6* associated with a decrease in height, resulting in increasing b/h and P/A, while triplets C and D are approximately constant. During *e7* an increase in area for triplet B is associated with an increase in height so that b/h and P/A decrease, while once again triplet C and D exhibit comparable behavior. During *e8*, triplet B approaches an equilateral configuration as the beacons approach the ice edge; increased stretching is observed for triplet C relative to triplet D continues. P/A and b/h thus provide a signature of stretching and ice drift response to the coastline, the relative contributions of which are further described by deformation and DKPs.

Figure 7. Sea ice deformation

Sea ice deformation during sudden changes highlights differences in sea ice response based on distance from the continental coastline. In particular, during *e1* triplet A is characterized by dominant contributions from vorticity, shear, and to a lesser extent, divergence, whereas triplet B witnessed a decline in shear and vorticity. Triplet C witnessed a decline in shear and transition to predominantly anticyclonic activity accompanied by comparatively weak stretching, while triplet D experienced a transition to convergence and negative vorticity. During *e2*, Triplet B experiences a transition from vorticity and stretching to shear, while triplet C is governed by shear. DKPs for triplets A and D are comparatively weak. During *e3*, only triplet B exhibits a transition from shear to anticyclonic activity, in contrast to comparatively weak DKPs for all other triplets. It should be noted that a negative stretching deformation rate indicates stretching along the y-axis (meridional) and shrinking along the x-axis (zonal). Triplet B during *e4* is characterized by a transition from cyclonic activity to stretching along the x-axis, while triplet D is distinguished by vorticity and shear compared to triplets A and C, which exhibit weak deformation. Similarly during *e5*, weak DKPs are observed for triplet C, with triplets B and D governed by vorticity. During *e6*, triplet B is governed by meridional stretching, followed by zonal stretching and oscillatory motion in N until *e7* and 20 October, following which convergence and divergence dominate. During *e8*, triplet B is governed by vorticity associated with reversals in drift orientation, while triplet C is governed by weak DKPs, following which alternating cyclonic and anticylonic circulation is observed.

Figure 8. Relative sea ice deformation.

It is interesting to note that extrema in the Okubo-Weiss criterion roughly coincide with sudden changes in ice drift (Figure 8). In particular, during *e1*, triplet A is characterized by vorticity, while triplets C and D are characterized by deformation-dominated flow, and triplet B by shear (Figures 7 and 8). During *e2*, triplet A is governed by deformation (S and N), triplet B by divergence, triplet C by shear (Figures 7 and 8, and shear-to-divergence values ~90), and triplet D by divergence. During *e4*, triplet B is

governed by divergence, while during *e6*, triplet B is governed by deformation (N; Figures 7 and 8), and triplets C and D by divergence. During *e7*, triplet B is governed by divergence, as are triplets B to D to a lesser extent during *e8*.

5